FRICTION ANALYSIS AND MODELING IN METAL CUTTING PROCESSES AT ELEVATED TEMPERATURES

by

Zhenhua Tao

B.S. In M.E., Xi'an Jiaotong University, 1992

M.S. in M.E., Shanghai Jiaotong University, 1995

Submitted to the Graduate Faculty of

the School of Engineering in partial fulfillment

of the requirements for the degree of

Doctor of Philosophy

University of Pittsburgh

2002

UNIVERSITY OF PITTSBURGH

SCHOOL OF ENGINEERING

This dissertation was presented

by

Zhenhua Tao

It was defended on

Dec. 9, 2002

and approved by

Michael R. Lovell, Associate Professor, Department of Mechanical Engineering

Scott X. Mao, Professor, Department of Mechanical Engineering

Frederick S. Pettit, Professor, Department of Materials Science and Engineering

William S. Slaughter, Associate Professor, Department of Mechanical Engineering

Qing-Ming Wang, Assistant Professor, Department of Mechanical Engineering

Dissertation Director: Michael R. Lovell, Associate Professor, Department of Mechanical Engineering

ABSTRACT

FRICTION ANALYSIS AND MODELING IN METAL CUTTING PROCESSES AT ELEVATED TEMPERATURES

Zhenhua Tao, PhD

University of Pittsburgh, 2002

Friction is a critical factor in determining the quality of metal cutting operations. In this work, influences of workpiece material properties and the real area of contact on interfacial friction were analytically investigated at elevated temperatures. From the analytical results, the yield strength of the workpiece material was found to not only directly influence the friction as indicated by Challen and Oxley's model, but also indirectly influence the friction by changing the real contact area. An rigid plastic model for tool/workpiece real contact area was proposed which showed that the real contact area and the average asperity slope angle increased significantly at elevated temperatures. Based on experiments conducted upon a specially designed experimental apparatus, influences of tool coating material and temperature on the friction in a metal cutting process were investigated. By the help of atomic force microscopy, it was found that the friction coefficient in the metal cutting process studied was directly related to the slope of the tool asperities, the real area of contact within the

tool/workpiece interface, and the level of asperity interaction. By varying the working temperature over a wide range of operating conditions, the microstructures of the workpiece materials and thermal properties of the tool coatings were found to significantly influence the friction coefficient. For the specific coating materials studied, Al_2O_3 was found to have the best friction and wear performance at higher temperature, while TiN performed better at the lower temperature examined. The TiC/TiN coated tools demonstrated a consistent performance with respect to friction over the range of temperature studied. Finally, an empirical model that related the friction to the yield strength of workpiece material was established and discussed.

DESCRIPTORS

Asperity
Friction coefficient
Real contact area
Shear flow stress
Slip-line field
Surface profile
Yield strength

ACKNOWLEDGEMENTS

At the time when my dissertation is ready, I'm so earnest to express my most sincere appreciation to all those who have given me great helps and supports during the preparation of the dissertation and throughout my PhD study.

I would like to express my gratitude to my advisor Dr. Michael R. Lovell for his guidance, advice, and support throughout the time. I would like to thank Dr. Frederick S. Pettit for not only serving on my committee but also providing me the facility for the experiment and giving me constructive advice. The efforts of Dr. Scott X. Mao, Dr. William S. Slaughter, and Dr. Qing-Ming Wang for serving on my committee are greatly appreciated.

I would also like to send my appreciation to so many friends and specialists. Thank Dr. Ning Fang for his advice on designing experiments. Thank Dr. Wen Gao, Ms. Li Cao for their guidance and help on preparing samples. Thank Dr. Nianqiang Wu and Dr. Xiaodong Han for their patient instructions in material fields. Thank all those who helped me in tests and measurements.

A special thank and all my love are given to my wife, for your attentive care, for your encouragement in my frustrating situation, for your smile all the time, and for your warm heart that is always surrounding me. Thank my father, my sister, my parents-in-law, and my sisters and brothers-in-law for their understanding and support.

TABLE OF CONTENTS

Page

LIST OF TABLES

Page

LIST OF FIGURES

Page

1.0 INTRODUCTION

1.1 Background

Being an integral factor in metal cutting operations, the friction generated by a hardened cutting tool sliding relative to a softer workpiece material is not completely understood. This is primarily due to the fact that the friction between the tool and the workpiece is a complicated function of several interrelated variables. As shown in a typical cutting process depicted in Figure 1.1, the tool-workpiece interfacial friction is dependent on temperature, surface properties, operating conditions (rate, depth of cut, etc.), lubrication, tool material and geometry, and workpiece material. Creating a better understanding of the friction in the tool-workpiece interfacial region is essential because friction often controls the quality of the material removal in machining processes. Friction can directly influence the workpiece final surface finish, the chip thickness, the chip flow direction, the required cutting force, and the temperature rise in the cutting tool. Better characterization of friction can also lead to a better fundamental understanding of a several second order variables such as the deformations in the primary and secondary shear planes, the heat generated along the clearance face of the cutting tool, the tool wear rate, and ultimately the likelihood of tool failure.

Despite the important contributions made by the metal working friction models available in the literature, many variables (temperature, velocity etc.) that influence the dynamic nature of friction in metal cutting need further investigation. By creating a better understanding of the friction involved, it is believed that manufacturers will be better

able to attain the stringent design tolerances and production efficiency demanded by the current industrial marketplace.

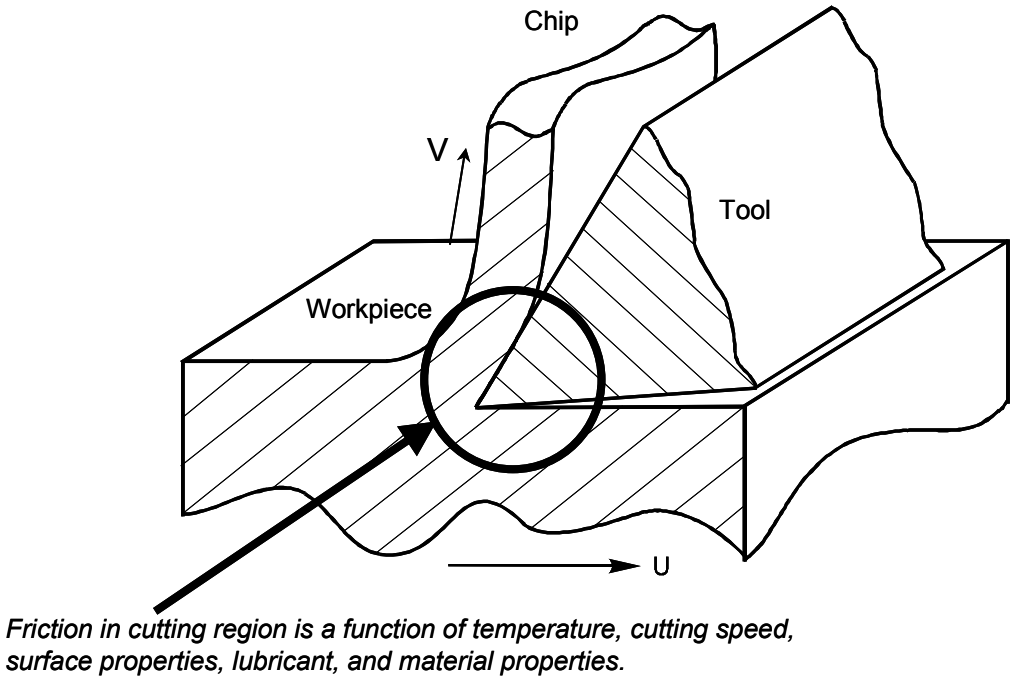

Figure 1.1 Illustration of Machining Process

1.2 Research Objectives

Metal cutting processes are always accompanied by high temperature. At high temperatures, friction between the tool and the workpiece will increase significantly comparing to that of at room temperature because of the change of the workpiece material properties. The increase of friction will in turn produce more heat that raises the temperature of the contact interface. As a result, friction at high temperatures is a critical

factor in the metal cutting processes. Exploring the mechanism of friction can lead to effective control of the metal cutting processes. In both analytical and numerical modeling, friction is an important parameter. Investigation of the friction at elevated temperatures is crucial for the analysis of metal cutting, especially for thermal modeling of metal cutting processes.

The objectives of present research are to investigate the friction between the cutting tool and the workpiece at elevated temperatures. By analyzing individual parameters, critical factors in the friction magnitude will be ascertained and discussed. The investigation concerns both the cutting tool and the workpiece. The relationship between the mechanical properties of the workpiece at elevated temperatures and the friction are the initial focus of the present work. The cutting tool surface profile will also be analyzed. By estimating the real contact area at different temperatures, the relationship between the average asperity slope angle and friction will be determined. Finally, an empirical expression on the friction at elevated temperatures will be developed. Such a relationship is useful for analytical and numerical analysis of metal cutting processes.

The outline of the remainder of this dissertation will proceed as following. In order to give a sufficient background on the subject matter, a summery of metal cutting theories including cutting models, friction models, temperature in metal cutting process, and coating technologies will be reviewed in Chapter 2.0. Analysis of friction-influence factors at elevated temperatures will be presented in Chapter 3.0. A detailed description is then provided in Chapter 4.0 of the experimental apparatus and the operating procedure utilized in this research. The experimental friction results are discussed in

Chapter 5.0 where the friction coefficient is plotted as a function of the process variables. An empirical formula for the friction is also derived in Chapter 5.0. In Chapter 6.0, conclusions are drawn based upon the evidences obtained from the experiments and analyses.

2.0 LITERATURE REVIEW

A Systematic review of metal cutting processes will be presented in this chapter. Modeling of metal cutting processes will be reviewed first. Friction models in metal cutting in different stages will follow. Coating technologies and the impact on metal cutting processes are then introduced. Temperature distribution in cutting tool will finally be discussed.

2.1 Cutting Process Models

2.1.1 Analytical Models

The early theoretical analysis of cutting processes was started from shear plane deformation [1-3]. This analysis was based on the orthogonal cutting and continuous chip assumptions. In the model, the chip contacts closely with the rake face of the tool near the tool tip and flows up along the tool rake face, until eventually it leaves the tool rake face by curving. There is always a shear plane (see Figure 2.1) between the chip and the workpiece. Determining the shear angle is a key component of this model. By minimizing the shear energy, it is found

$$\phi = \frac{\pi}{4} - \frac{1}{2}(\varphi - \gamma) \qquad (2.1)$$

where ϕ is shear plane angle, γ is the rake angle of the cutting tool, and φ is the friction angle in Figure 2.1. In practice, the shear plane is actually a zone with finite thickness (primary shear zone).

Equation (2.1) is an idealized model and doesn't explain the interfacial friction in metal cutting. Rowe and Wolstencroft [4] introduced the secondary shear zone model to overcome the problem. They proposed the existence of the second zone which is a heat source during the metal cutting processes. With the consideration of the secondary shear zone, the shear plane angle ϕ can be calculated from the following equation:

$$k_1 \cos\gamma \cos(2\phi - \gamma) = \beta\omega k_2 \sin\phi \qquad (2.2)$$

where k_1 is the shear flow stress in the first zone, k_2 is the material shear flow stress in the second zone, β, and ω are parameters which can be obtained from experiments. The value of β is directly related to the friction in the secondary zone. When lubricant is applied in the cutting processes, β is small. Otherwise, β can become large. From the equation, large values of β give small ϕ (primary shear angle) and vise versa.

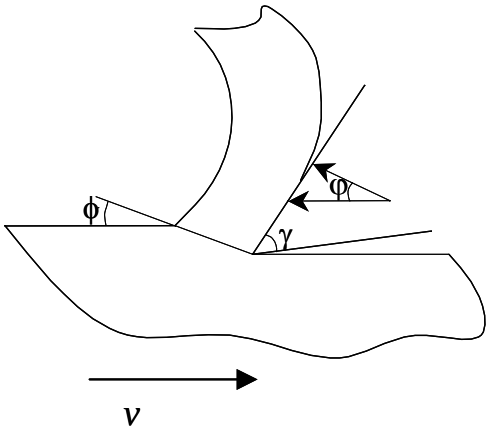

Figure 2.1 Merchant's Cutting Model

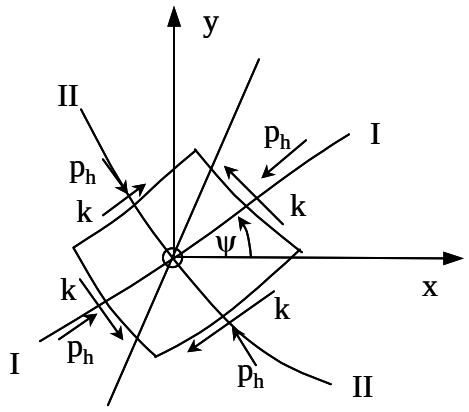

Figure 2.2 Slip-Line Fields in an Element

A second analysis used to model the friction in the cutting process was the slip-line field theory. The slip-line field theory was initially developed for the plastic analysis of the metal before being introduced into cutting processes. In this research field, Oxley and his co-workers made systematical contributions. A slip-line field is a plastic zone in which two sets (sets I and II) of curvilinear slip-lines (loci of the directions of maximum shear flow stress) are perpendicular with each other (see Figure 2.2). The following Equations are held by the equilibrium requirement [5].

$$\begin{cases} p_h + 2k\psi = \text{const along I line} \\ p_h - 2k\psi = \text{const along II line} \end{cases} \qquad (2.3)$$

where p_h is the hydrostatic stress within the field, k is the shear flow stress of the workpiece material, and ψ is the angle of the tangent line of slip-line I off the x axis of coordinate system. Considering the work hardening factor, the above Equations become [6]:

$$\begin{cases} p_h + 2k\psi + \int \frac{\partial k}{\partial s_2} ds_1 = \text{const along I line} \\ p_h - 2k\psi + \int \frac{\partial k}{\partial s_1} ds_2 = \text{const along II line} \end{cases} \qquad (2.4)$$

where ds_1 and ds_2 are elemental lengths of the slip-lines.

Using the slip-line theory, Oxley and co-workers developed the models for both the thin shear zone and the thick shear zone analysis. The thin shear zone model simplifies the shear zone to a parallel sided slip-line field with very small thickness (see Figure 2.3 (a)). The relationship between the shear angle and other parameters is expressed as [6]:

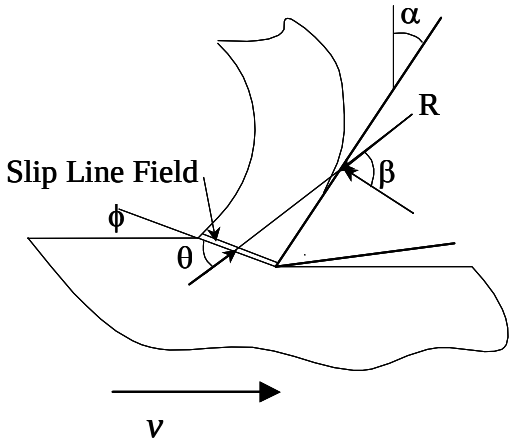

(a) Thin shear zone

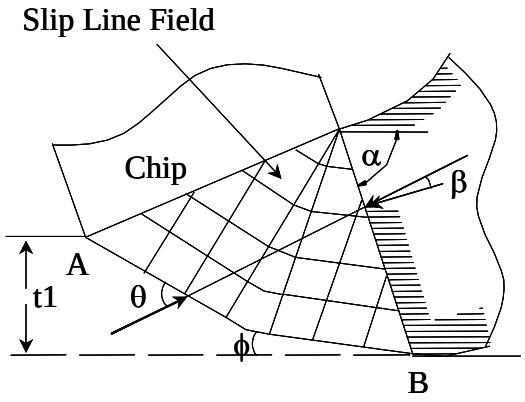

(b) Thick shear zone

Figure 2.3 Slip-Line Cutting Models

$$\begin{cases} \theta = a\tan\left(\dfrac{1}{2} + \dfrac{\pi}{4} - \phi + \dfrac{\cos(2*(\phi-\alpha))}{2\tan\beta} - \dfrac{\sin(2*(\phi-\alpha))}{2}\right) \\ \theta = \phi + \beta - \alpha \end{cases} \qquad (2.5)$$

Where α is the rake angle of the cutting tool, β is the friction angle, and θ is the angle between the resultant cutting force and the shear plane.

The thick shear zone model is more physically realistic but more complicated to apply. Palmer and Oxely [7] constructed the thick slip-line model (see Figure 2.3(b)). In this model, an irregular shear field exists between the workpiece and the chip. Using the fundamental slip-line relations, the following expressions are obtained [7]:

$$\begin{cases} \phi = \theta + \alpha - \beta \\ \tan\theta = A_1 - A_2 + \dfrac{A_1 - P_1/k}{\exp(A_1 - P_1/k)/A_2 - 1} \end{cases} \qquad (2.6)$$

where

$$\begin{aligned} A_1 &= 1 + 2\left(\frac{\pi}{4} - \phi\right) \\ A_2 &= \cot\phi - \tan\theta \end{aligned} \quad . \qquad (2.7)$$

k is the shear flow stress along AB in Figure 2.3 (b), and the hydrostatic stress at B (P_1) can be determined from *k*, θ, and ϕ.

Estimates of the secondary shear zone were also made by Roth and Oxley [6] using slip-line method.

2.1.2 FEM Models

Other than analytical methods, FEM is another effective tool which is used in the cutting process analysis. The cutting process analysis using FEM began in the 1970s. In the early stages, the FEM models (Zienkiewicz [7], Kakino [8]) were rather simple. They were two dimensional cutting process simulations that assumed no friction between the cutting tool and the workpiece. The chip shape was predicted before the calculation. These limitations were overcome by Shirakashi and Usai[9]. Shirakashi and Usai used ICM (Iterative Convergence Method) to change the shape of the chip dynamically and obtained a realistic solution. A Sticking-sliding friction model was developed by Shih [10] using an unbalanced force reduction method. Non-steady chip formation analysis was realized by Strenkowski & Carrol [11]. After the rigid-perfect three-dimensional model [12] was used to simulate the chip formation, an elastic-plastic three-dimensional steady state model [13] and non-steady state model [14] were realized in cutting simulation.

2.2 Friction Models

2.2.1 Adhesion Friction Models

Reviewing the literature, several theoretical models have been proposed for analyzing the friction encountered during metal cutting processes. The adhesion model was first applied to metalworking in 1939 by Bowden and Tabor [15-16]. Bowden and Tabor demonstrated that the real area of contact could be much smaller than the apparent

area of contact and that the real area could vary with the normal load and the hardness of the contacting (tool and workpiece) surfaces. They defined the frictional force as the force required to shear the welded junctions formed by adhesion at the tips of the asperities on contacting surfaces. According to their model, interfacial sliding would only occur if the shear stresses generated by a tangential force were sufficient to overcome the shear strength of the interfacial film:

$$\mu = \frac{1}{\delta^{1/2}(f^{-2} - 1)^{1/2}} \qquad (2.8)$$

In Equation (2.8), f is the normalized film strength given by $f = \tau/k$. τ is the shear strength of the film, k is the shear flow stress of the deforming material, and δ is an empirical factor taken to be 9. Green [17-18] later examined the asperity deformation model in detail using advanced plasticity theory. He contented that during junction growth the friction coefficient could be taken as the ratio between the average tangential and normal forces acting over the life cycle of a typical junction. He demonstrated how the normal stress could become tensile near the end of the life cycle, thereby causing fracture of the junction.

2.2.2 Asperity Deformation Models

While the adhesion model promoted to a considerable degree a better understanding of the mechanisms involved in friction of metal working processes, it laid too much emphasis on fracture of asperities. The theory of formation and shearing of welds is not justified, for instance, in cases where one surface (cutting tool) is considerably harder

than the other surface (soft workpiece). To overcome limitations in the adhesion model for metal cutting processes, Challen & Oxley [5] introduced the slip-line field models for asperity deformations. According to Challen & Oxley, the friction is brought about from the plastic deformation of the soft material. Based on the assumption that the deformation is restricted by plane strain and the workpiece is volume constant, Challen & Oxley proposed three different friction models for metal cutting processes: (1) abrasion, (2) wear, and (3) cutting. The difference between these models lies in the severity of the contact conditions which is controlled by the asperity wedge angle, α, and the free surface angle, η (see Figure 2.4).

The abrasion model is the most fundamental among the three models. It has been proposed [5] and then observed in the experiment [19] that there exists a plastic field (slip-line field) under the contact region of the tool. Using the geometry relations (Figure 2.4 (a)) and velocity discontinuity relationships (see Figure 2.4(b)), the following equations are obtained:

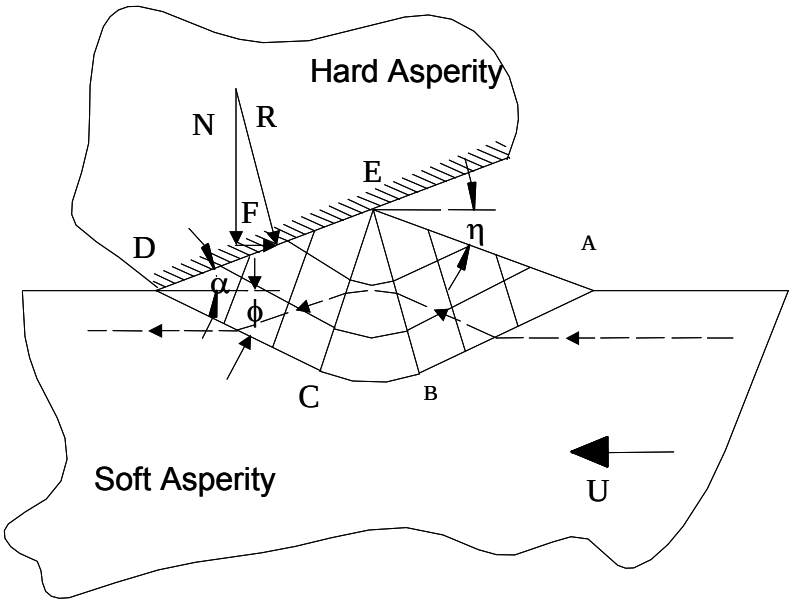

(a) slip-line field

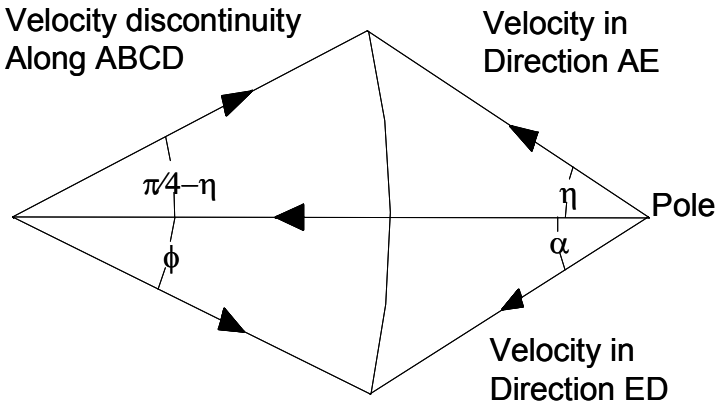

(b) Hodograph

Figure 2.4 Plastic Deformation (a) Slip-Line Field (b) Hodograph

$$\begin{cases} f = \cos 2(\alpha + \phi) \\ \sin\alpha = \sin\eta \times \sqrt{(1-f)} \end{cases} \qquad (2.9)$$

where *f* is defined as the ratio of shear stress , τ, along contact surface DE to the shear flow stress, *k*, of the workpiece material, and ϕ is the angle between slip-line CD and the moving direction of the workpiece. The hydrostatic stress p is related to the shear flow stress in the form:

$$p = k[1 + 2(\frac{\pi}{4} + \phi - \eta)] \qquad (2.10)$$

The horizontal and vertical components of the applied force R on the hard asperity are

$$\begin{cases} F = k[1 + 2(\frac{\pi}{4} + \phi - \eta)]\sin\alpha + \cos(\alpha + 2\phi)]L_{ED} \\ N = k[1 + 2(\frac{\pi}{4} + \phi - \eta)]\cos\alpha + \sin(\alpha + 2\phi)]L_{ED} \end{cases} \qquad (2.11)$$

respectively. The friction coefficient, from its definition, is obtained in the form:

$$\mu = \frac{F}{N} = \frac{A\sin\alpha + \cos(\cos^{-1} f - \alpha)}{A\cos\alpha + \sin(\cos^{-1} f - \alpha)} \qquad (2.12)$$

Where

$$A = 1 + \frac{\pi}{2} + \cos^{-1} f - 2\alpha - 2\sin^{-1}\frac{\sin\alpha}{\sqrt{1-f}} \qquad (2.13)$$

Friction coefficient (μ) as a function of α and *f* is plotted in Figure 2.5.

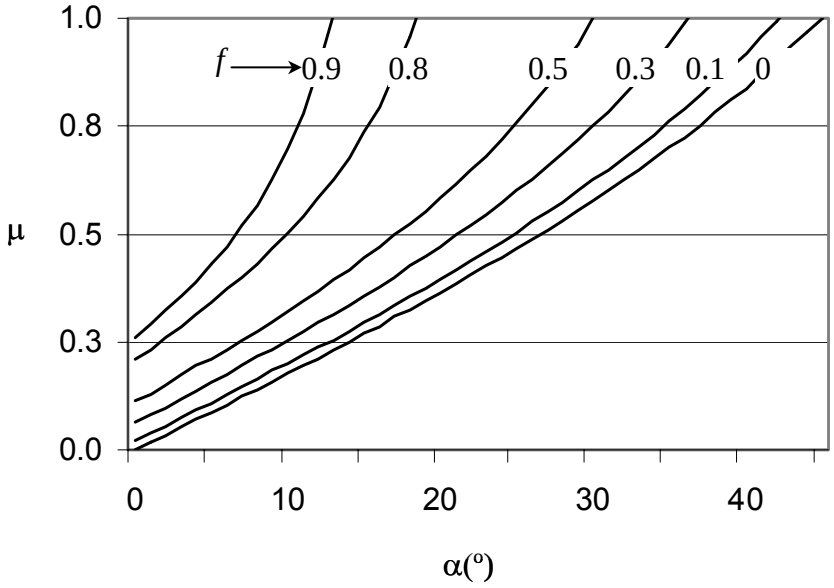

Figure 2.5 Friction Coefficient Variation with alpha and f

When η is larger than $\pi/4$, the geometry relationship in Figure 2.4(a) becomes invalid and the velocity discontinuity relationship break down. In this case, a steady state slip-line field doesn't exist. Fracture will develop and small grains will be produced in the process that is known as the wear model.

In both the abrasion and the wear model, the hard asperity angle (α) is less than $\pi/4$. In the situation when $\alpha>\pi/4$, the asperity acts as a cutting tool and chips will develop. This case is discussed in Section 2.1 and identified as the cutting model by Challen and Oxley. There are numerous publications that have experimentally verified slip-line friction models[19-23]. These experiments investigated the influence of wedge angle (5° to 120°) and operating conditions (lubricant, velocity, and surface roughness). In Challen

and Oxley's experiments, α and *f* were found to be the two key parameters in metal cutting processes. It is important to note that in Challen and Oxley's model, more emphasis was put on the angle of the hard wedge and factors which affect the shear stress (such as lubricant). The physical and mechanical properties of the soft material, however, were not a point of emphasis in their work.

2.2.3 Seizure Based Friction Models

Other researchers, such as Trent [24], have indicated that seizure, rather than asperity deformation, is a necessary condition in machining. Trent [24-25] defined seizure as *the interlocking and atomic bonding between the tool and workpiece material over most of the apparent contact area*. Under conditions of seizure, the tool and work materials essentially become one piece of metal along the contact interface so that the formation of new surfaces can only occur by the fracture of atoms. In the seizure model, the inter-atomic forces are believed to greatly retard the rate of movement of the work material over the tool and the workpiece velocity will approach zero near the seized contact interface. Similar to the asperity deformation model, Trent [25] used machining experiments as a basis for his seizure model. Trent noted that residual workpiece material left behind on both the peaks and valleys of the tool rake face near the cutting edge indicated that 'normal' (asperity deformation) sliding contact could not have occurred because of the continuous contact in the valleys of the tool.

2.2.4 Combined Adhesion and Sliding Models

As suggested by a number of researchers, it is likely that the friction along the tool-workpiece interface is a combination of asperity deformation and seizure. Based on experiments with flat-faced tools, (Boothroyd[26], Zorev[27], and Trent[28]), the tool-chip interface has been found to contain both adhesive (seizure) and sliding (asperity deformation) regions (see Figure 2.6). In Boothroyd's and Zorev's work, metal cutting was found to create an entirely new surface, which in the absence of lubricants and contaminants, was an ideal condition for adhesion contact at increased temperatures. Thus, as the tool contacted the workpiece, the workpiece material adhered to the tool face and shear occurred within the chip. During adhesion, the frictional force was found to be very high and a large amount of frictional heat was generated. In some case, as found by Boothroyd and Trent, there is strong enough adhesion between the tool and the workpiece so that the actual layer of the chip on the rake face will be arrested and the chip velocity will occur in a narrow secondary deformation zone between points A and C. As depicted in Figure 2.6, however, Boothroyd's and Trent's experiments have also shown that not all of the tool-chip contact interface is adhesive. As the cutting tool penetrates the workpiece, physical separation occurs between the tool and the chip at the leading edge of the contact interface. Just prior to separation, the normal forces between the tool and the chip decrease and the contact along the cutting tool becomes predominantly sliding in nature. Sliding friction, which is necessitated by separation of the tool and chip, is characterized by a region of decreasing frictional forces which

diminishes altogether as the chip departs from the cutting tool. In the cutting of a chip of finite length, Boothroyd and Zorev have found that this sliding region (from B to C) surrounds the adhesion zone (from tool tip A to B). There also exists a transitional region along the tool-chip interface which is defined by intermittent sliding and adhesive friction. Whether the size of the transition region is small, as suggested by Wallace and Boothroyd [29], or large, as found by Finnie and Shaw [30], likely depends on the particular materials and operating conditions.

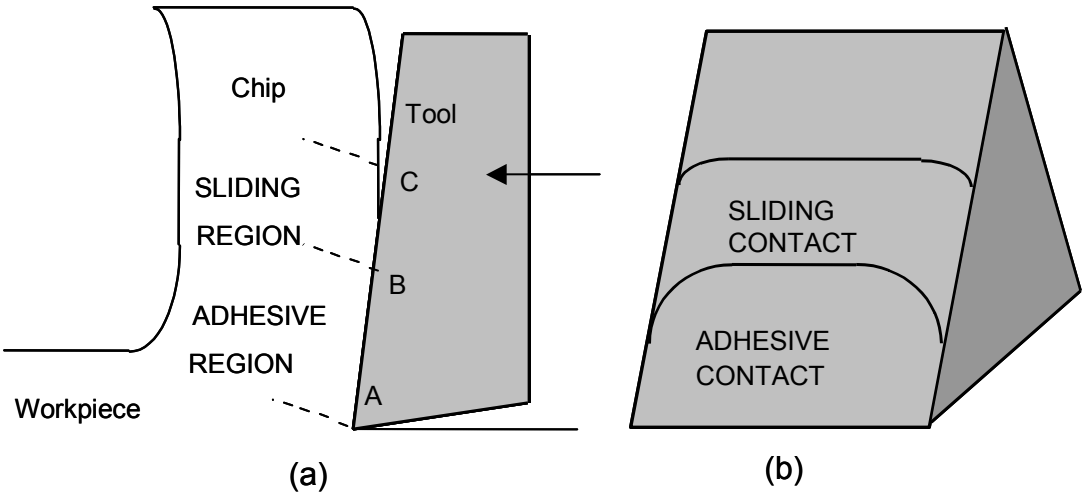

Figure 2.6 Zones of Contact along the Tool-Workpiece Interface

2.2.5 Empirical Models

In addition to the adhesion, asperity deformation, and seizure models, the variability of the friction coefficient with cutting condition has alternatively been modeled using a characteristic stress equation for the tool-chip interface. In these models, the friction stress boundary conditions are applied for the tool-chip interaction. Shirakashi and Usui [31] first developed a friction stress and normal load empirical relationship using:

$$\tau_t = k\left(1 - e^{-\lambda\frac{\sigma_n}{k}}\right). \qquad (2.14)$$

In Equation (2.14) τ_t and σ_n are respectively the frictional and normal stresses, k is the shear flow stress of the chip, and λ is a constant fitting the curve of the friction stress versus the normal stress at the tool rake face. The parameter λ depends on the chip-tool material combination.

2.3 Coating Technology

One of the most revolutionary changes in the metal cutting industry over the past thirty years has been the application of coatings onto the cutting tool. More than half of the cutting tools produced today are coated with a thin hard film (or multiplayer films) of wear resistant material [32]. As a general principal [33], the lifetime of a cutting tool is significantly prolonged when a coating is applied. The type and number of coating

materials can be varied to obtain optimum cutting attributes for a specific workpiece material and cutting condition. In the manufacturing industry, the typical coating material used for tool inserts are TiC, TiN, and Al_2O_3. TiC and Al_2O_3 have good chemical stability and ultrahigh hardness which can increases the wear resistance. TiN, in contrast, provides lower friction to the face of the tool insert which can substantially reduce cratering of the cutting tool [34]. For most materials, the thermal conductivity increases with increasing of the temperature. Al_2O_3, However, possesses special thermal properties. It's thermal conductivity decreases at elevated temperatures (see Figure 2.7). As a result, Al_2O_3 provides a strong heat barrier between the cutting tool and the workpiece and chip [35]. Multilayer coating can combine the advantages of different coating materials. Accordingly, multilayer coating can obtain better performance over single layer coatings [36]. It is reported that the multilayer coating are more shock resistive [37]. Hence, depending on the operating conditions, different tool coating can be used to significantly alter cutting performance.

Reviewing the literature, substantial work has been performed to investigate the role of tool coatings in material cutting operations. In these publications, the performances of tool coatings have been primarily evaluated as a function of the cutting speed, normal pressure and temperature [38,39]. The variation of tool friction and wear has also been determined as a function of the mechanical and tribological properties of the coating materials [40]. Differences between multilayer and single layer coatings have been examined and it has been found that multilayer coatings can exhibit better friction and wear properties than that with single layer [41]. In work by Lovell et al., the temperature fields and stress distribution in coated cutting tools have been analyzed [35,42].

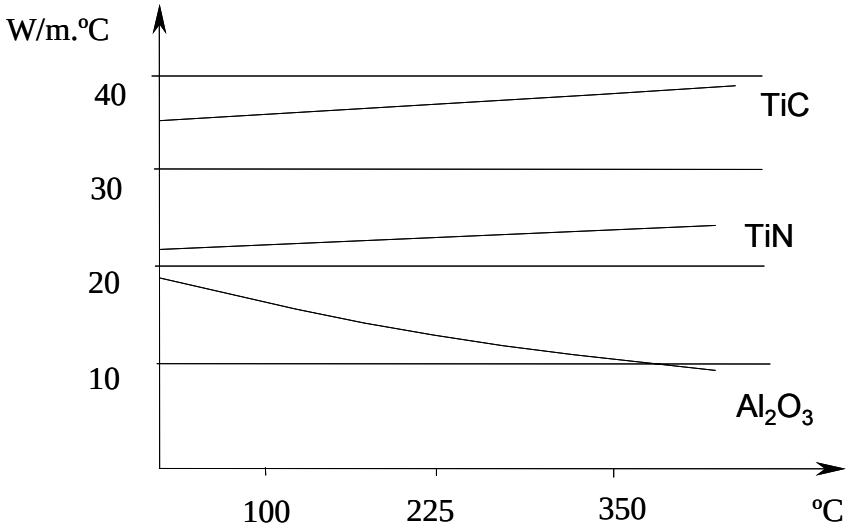

Figure 2.7 Thermal Conductivity as a Function of Temperature for Selected Materials

2.4 Temperature in Machining Processes

Since establishing the influence of temperature on the friction in metal cutting operations is one of the primary focuses of this research, it is pertinent to review the character of the interfacial temperature in metal cutting operations. Considering the temperature rise along the contact interface, there are three main regions (see Figure 2.6) of heat generation in machining: (1) the primary deformation zone where the chip is formed, (2) the secondary deformation zone where the chip slides over the cutting tool face, and (3) the area where the machined surface contacts the clearance face (flank) of the tool. Due to these complex heat generation mechanisms, the temperature along the cutting interface is not uniform. In fact, as shown in Figure 2.8 [43], the maximum temperature typically occurs slightly below sliding/adhesion friction interface. In any

metal working process, the temperature along the contacting interface varies due to the combined influence of bulk heat generation effects and the local abrasion and plastic deformation of the tool-workpiece asperities. Localized temperature variations can substantially change the material properties along the contact interface, especially for the softer (workpiece) material. Since a material's yield strength, shear strength, and hardness are all influenced by the operating temperature, the frictional interaction of a metal cutting process is highly dependent on temperature. Despite the fact that the temperature profile (see Figure 2.8) has been studied along the tool-workpiece interface for more than fifty years, no metal cutting friction models currently exist that are a direct function of temperature. Developing such a model is important, especially with the current trends towards utilizing finite element methods for predicting the machining behavior. In the finite element method, cutting temperatures are known at integration points and/or nodal locations along the tool/workpiece interface. Generating temperature dependent friction model, therefore, would allow the friction along the tool/workpiece interface to vary locally, as is the case in an actual machining process.

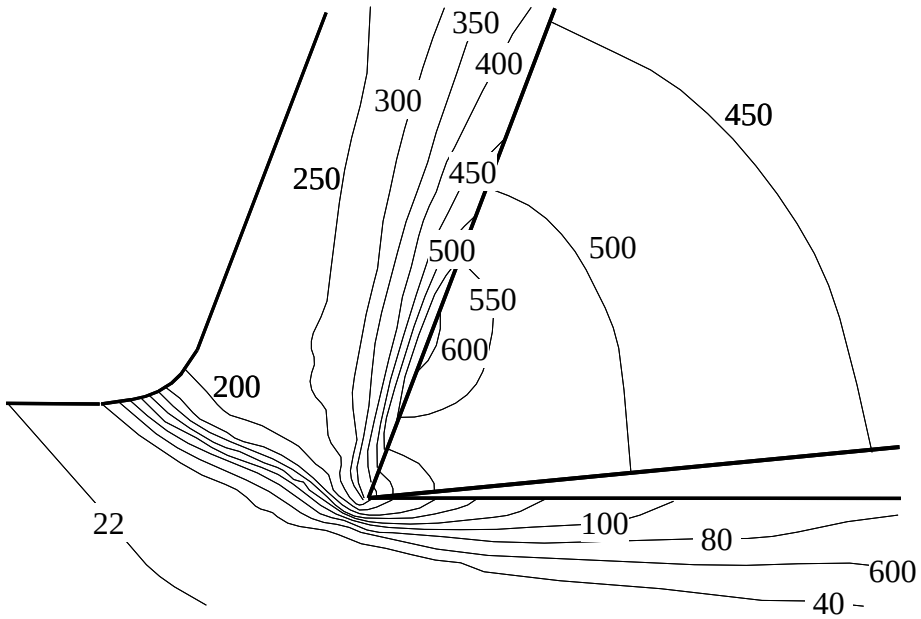

Figure 2.8 Temperature Profile for Orthogonal Machining of Al 2011

3.0 FRICTION ANALYSIS AT ELEVATED TEMPERATURES

3.1 Material Microstructure Change at Elevated Temperatures

In this section, the change of mechanical properties with temperature will be discussed for several alloys. The temperature range within the discussion is from room temperature to 400°C, which as will be discussed later can be obtained in our experiment.

At elevated temperatures, the variations in friction can be brought by the change of the microstructure of the workpiece materials. This is due to the fact that the microstructure (phase, grain size, and precipitates) of a material determines its mechanical properties. Some alloys, such as A48 class 40 gray iron, 80-55-06 ductile iron, and commercial-purity grade 2 titanium, have a stable microstructure within the range from room temperature to 400°C. Mechanical properties of Iron alloys are decided by the cooling speed and the components in the alloy since different speed can produce different microstructure. For the as-cast A48 class 40 gray iron and grade 80-55-06 ductile iron we choose in the tests, the microstructures (see Figure 3.1 [44]) are close to equilibrium conditions. When heated again to 400°C, which is far lower than the first phase change temperature 723°C (see Figure 3.2), there won't be marked change in the microstructure. Commercial-purity grade 2 annealed titanium, similarly, has the stable α phase (see Figure 3.3 [45]). Within the range from room temperature to 400°C, which is also far from the phase change (see Figure 3.4), there is only limited grain size change. As a result, the microstructure and the subsequent yield stress of gray iron, ductile iron,

and titanium remain essentially constant, which ultimately causes a less significant variation of the yield stress (see Figure 3.5 [46-48]) and friction with temperature.

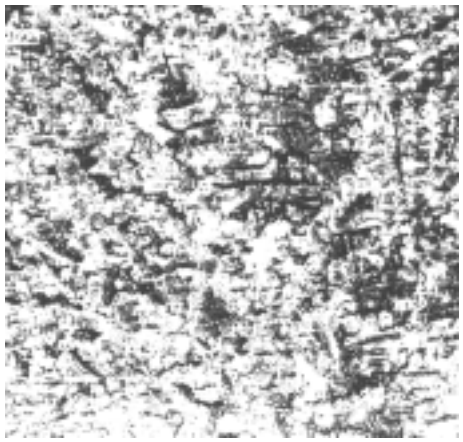

(a) A48 Class 40 Gray Iron

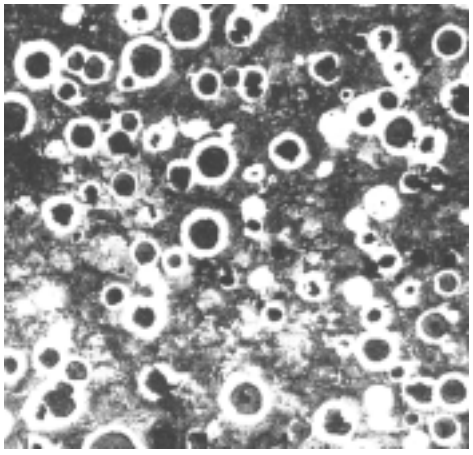

(b) 80-55-06 Ductile Iron

Figure 3.1 Iron Microstructures

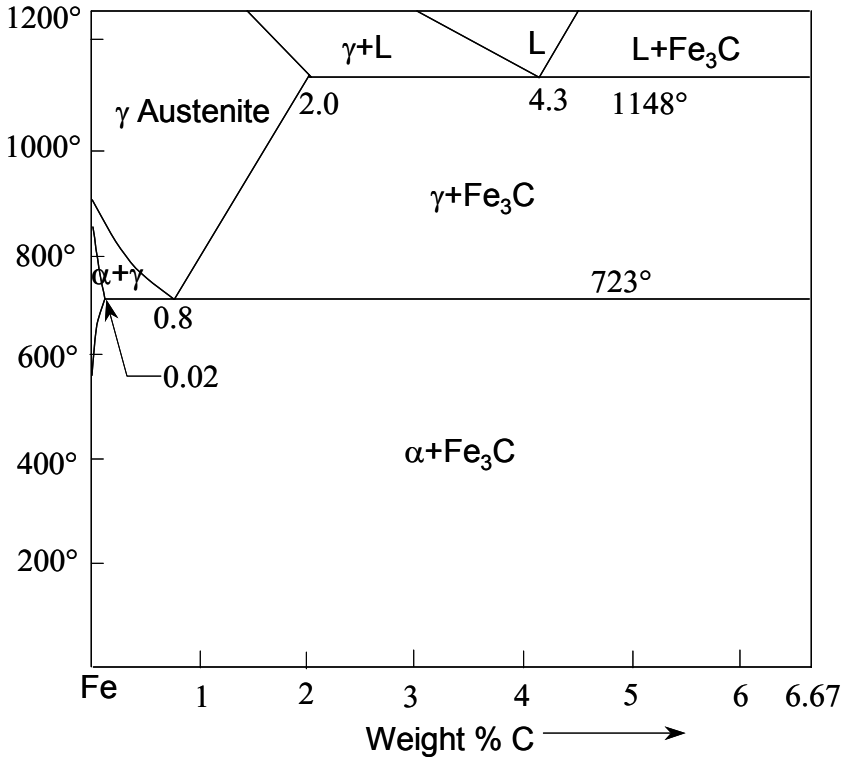

Figure 3.2 Fe-Fe_3C System

Figure 3.3 Microstructure of Commercial-purity Titanium

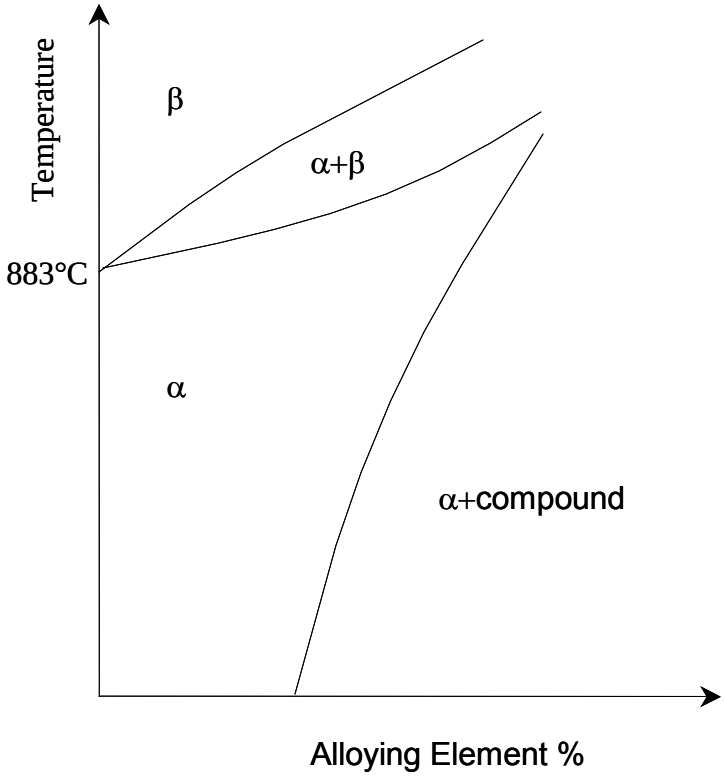

Figure 3.4 Titanium Stabilized System

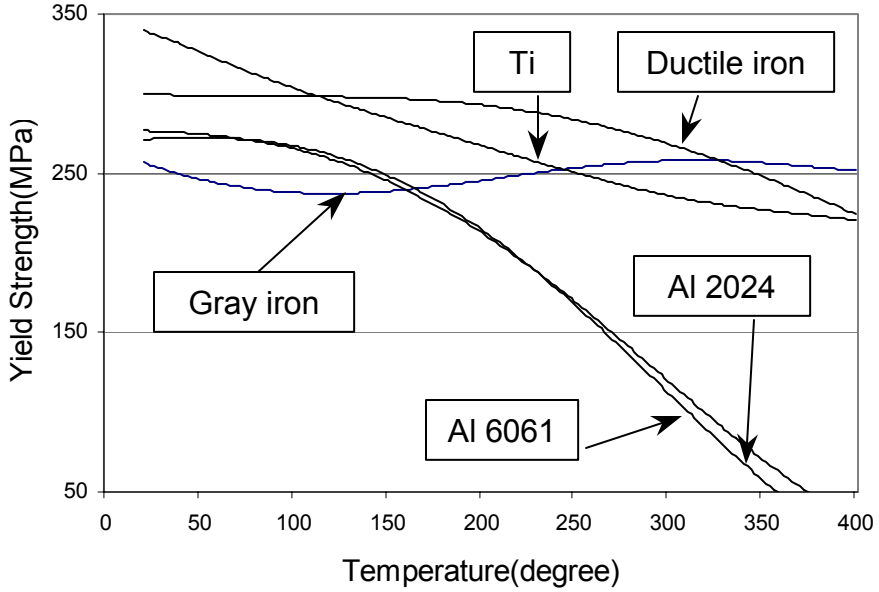

Figure 3.5 The Yield Strength Changing with Temperature

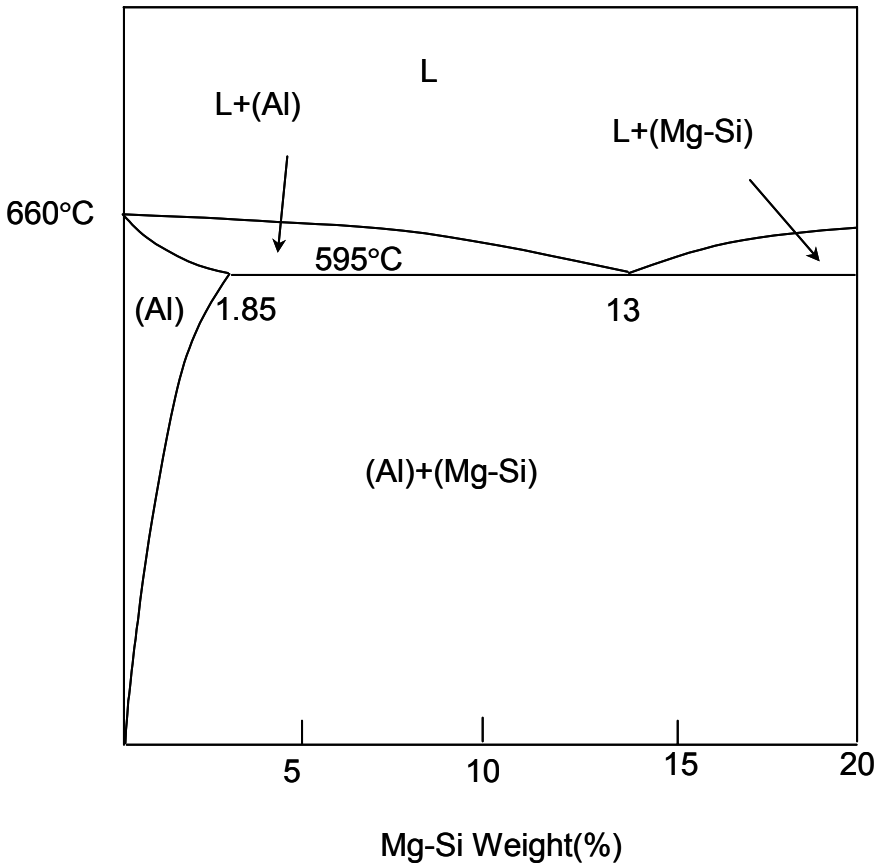

Figure 3.6 Al-Mg-Si phase Diagram

In contrast to the above alloys, Aluminum alloys undergo substantial change of mechanical properties at elevated temperatures because of complicated microstructure phase transformation. Al 6061 is an Al -Mg (1.1%)-Si (0.68%) alloy. 1.5% Mg_2Si is included in Al 6061. At the eutectic temperature of 595°C, Mg_2Si in Al 6061 is totally dissolved in α-aluminum. With the temperature decreasing to the room temperature, the solubility of Mg_2Si in aluminum drops down to 0.1% (see Figure 3.6 [49]). When the alloy is solution treated at about 550°C and water quenched, supersaturated solution of Mg_2Si is produced. Tempered then at 175°C for several hours, the microstructure dramatically changed. Although the process hasn't been totally understood, it's widely believed that Guinier-Preston (GP) zone is formed and high density Mg_2Si (β') (see Figure 3.7 and Figure 3.8) is obtained [50]. The mechanical properties remarkably improved. The process (solution treating, quenching, and aging) is T6 treating of aluminum. When the alloy is heated again to over 100°C, the GP zone converts to other forms (for example, from needle shape to rod shape). The converting speed increases with the temperature. The phase change weakens the alloy. The process continues until all β' form Mg_2Si transfers to the stable state. Similarly, Al 2024 T4 experiences the same process. Al 2024 is an alloy consisting of Al, Cu (4.5%), and Mg (1.5%). In this alloy, *S'* form Al_2CuMg will be precipitated (see Figure 3.9 [51]) after T4 treatment (solution treating, quenching, and naturally aging). At the elevated temperature, *S'* form phase will change to the equilibrium form (*S*) [50]. The phase transformation weakens the alloy, as in Al 6061 T6. The sharp decrease in the yield strength shown in Figure 3.5 reflects the phase transformation of Al 6061 T6 and Al 2024 T4.

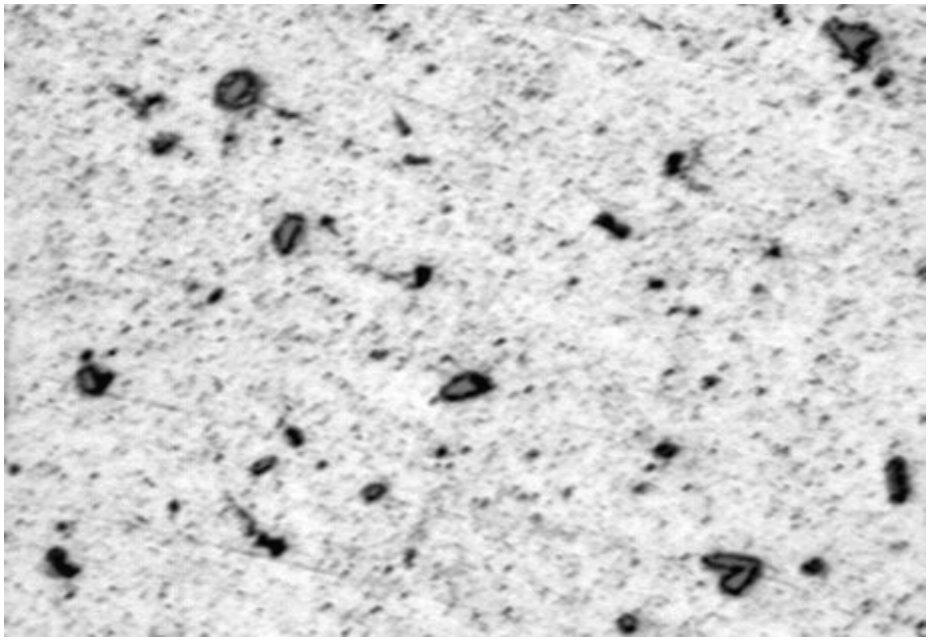

Figure 3.7 Microstructure of Al 6061T6 at Room Temperatures (×1000)

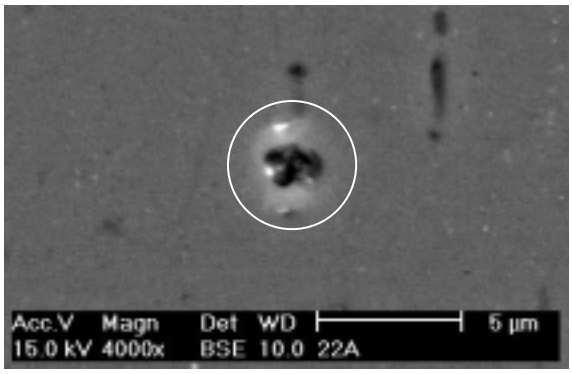

(a) SEM Image

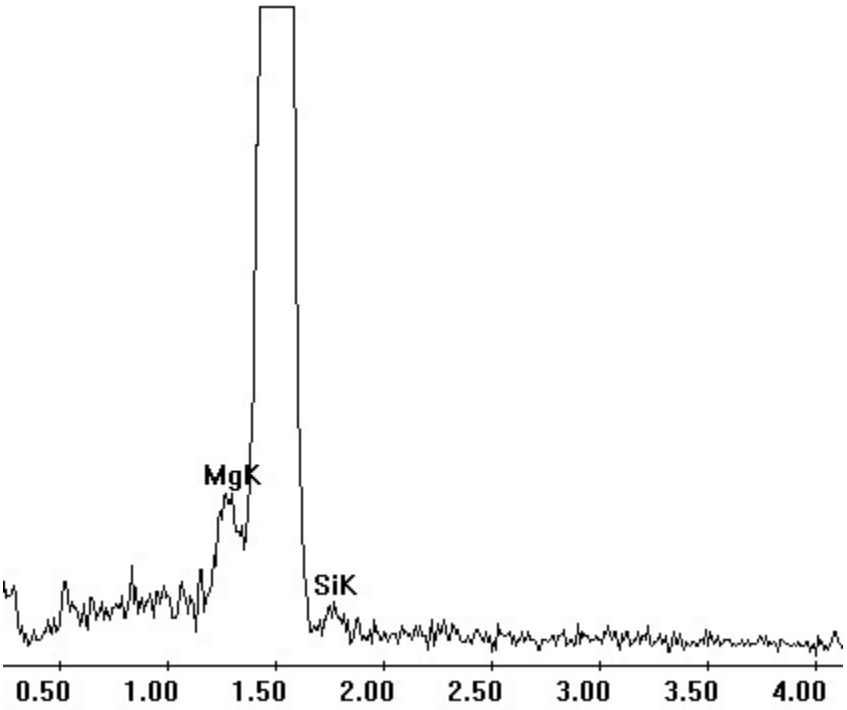

(b) Particle Identification

Figure 3.8 Identification of Mg_2Si in Al 6061 T6 (22°C)

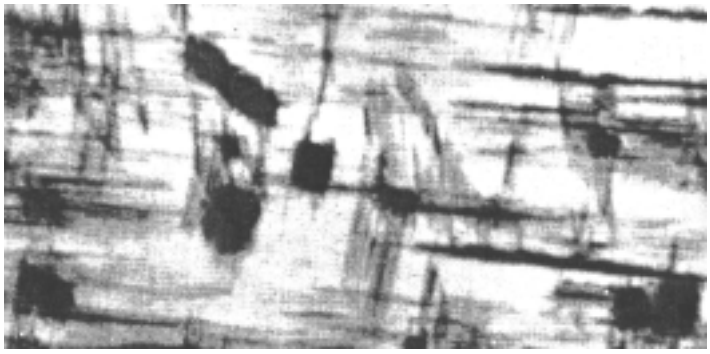

Figure 3.9 Al 2024, Solution Heat Treated, Quenched, Aged 12 hrs at 190°C

3.2 Statistical Simulation of the Tool Surface

In order to understand the role that tool coating materials have on the friction in machining processes, it is important to understand the asperity interaction along the tool-workpiece interface.

To characterize the surface condition, centerline average (R_a) is most commonly used. Centerline average is defined as

$$R_a = \frac{1}{L}\int_0^L |z(x)|dx\,, \qquad (3.1)$$

where *z(x)* is the surface profile function, and *L* is the length of the profile. It is important to note that R_a can only provide information in the vertical direction. In contact analysis, the slope angle of the single asperity is an important parameter which directly influences friction. The average slope in a given measured length (L) can be expressed as

$$\Delta_a = \frac{1}{L}\int_0^L \left|\frac{dz(x)}{dx}\right| dx\,. \qquad (3.2)$$

The curvature of the single asperity is another important parameter to describe the surface. The curvature is defined as:

$$\mathrm{K}_a = \frac{1}{L}\int_0^L \left|\frac{d^2 z(x)}{dx^2}\right| dx\,. \qquad (3.3)$$

Above parameters provide information of the average asperities. However, some other information, such as the distance of the adjacent asperities, is still undisclosed. Prior research [52] has revealed that the whole surface profile information can be sufficiently described by three moments (0^{th}, 2^{nd}, and 4^{th}) of the spectral density function (*G(k)*). The moments are

$$m_0 = \int_0^\infty G(k)\,dk \quad , \tag{3.4}$$

$$m_2 = \int_0^\infty k^2 G(k)\,dk \quad , \tag{3.5}$$

and

$$m_4 = \int_0^\infty k^4 G(k)\,dk \quad . \tag{3.6}$$

For the Gaussian distribution, the above moments can also be expressed as [52]

$$m_0 = \frac{1}{L}\int_0^L z(x)^2\,dx \quad , \tag{3.7}$$

$$m_2 = \frac{1}{L}\int_0^L \left(\frac{dz(x)}{dx}\right)^2 dx \quad , \tag{3.8}$$

and

$$m_4 = \frac{1}{L}\int_0^L \left(\frac{d^2 z(x)}{dx^2}\right)^2 dx \tag{3.9}$$

respectively.

On a digitally sampled data set, the above parameters can be obtained in the expressions that are listed in Table 3.1.

To calculate the real contact area, an asperity shape should be used to simplify the contact model. Spherical shapes were first used by Greenwood and Williamson [53] and widely accepted in contact analysis. In their analysis, Greenwood and Williamson presumed that all asperities were spherically shaped near their summits, and the radii of the summits were the same. In contrast, the heights of the summits varied.

Greenwood and Williamson's spherical model can successfully simulate the elastic (Hertz) surface contact. However, in metal cutting processes, the workpiece is assumed rigid-plastic. Tool/workpiece contact is obviously non-hertz contact. Moreover, the moments of the spectral density function of the shape which is used to simulate the real surface should conform the real surface. After comparing the statistical parameters with the measured real tool surface (see Table 3.2), it has been found that a cone can more realistically simulate the surface profile. For the different shapes in Table 3.2, the geometry of each entity is constructed from the shape parameters (R_a, Δ_a) of the real surface. For example, the height of the cone is set to $3R_a$ and the slope of the cone is set to Δ_a. Moreover, the geometries of the individual shape are assumed identical. The profile of the real measured surface (see Figure 3.10) also demonstrates that the surface summits are closer to cone shape rather than sphere shape.

Table 3.1 Surface Descriptors

	Description	Analytical Expression	Numerical Expression
1	Center line mean	$R_a = \frac{1}{L}\int_0^L \lvert z(x)\rvert dx$	$R_a = \frac{1}{N-1}\sum_{i=1}^{N} z_i(x_i)$
2	Slope	$\Delta_a = \frac{1}{L}\int_0^L \left\lvert \frac{dz(x)}{dx} \right\rvert dx$	$\Delta_a = \frac{1}{N-2}\sum_{i=2}^{N-1} \left\lvert \frac{1}{2}\left(\frac{z_{i+1}-z_i}{h} + \frac{z_i - z_{i-1}}{h} \right) \right\rvert$
3	Curvature	$\mathrm{K}_a = \frac{1}{L}\int_0^L \left\lvert \frac{d^2 z(x)}{dx^2} \right\rvert dx$	$\mathrm{K}_a = \frac{1}{N-2}\sum_{i=2}^{N-1} \left\lvert \frac{z_{i+1} - 2z_i + z_{i-1}}{h^2} \right\rvert$
4	0th order moment of arbitrary surface	$m_0 = \int_0^\infty G(k)dk$	$m_0 = \sum G(k_i) * \Delta h$
5	2nd order moment of arbitrary surface	$m_2 = \int_0^\infty k^2 G(k)dk$	$m_2 = \sum h_i^2 G(k_i) * \Delta h$
6	4th order moment of arbitrary surface	$m_4 = \int_0^\infty k^4 G(k)dk$	$m_4 = \sum h_i^4 G(k_i) * \Delta h$
7	0th order moment of Gaussian surface	$m_0 = \frac{1}{L}\int_0^L z(x)^2 dx$	$m_0 = \frac{1}{N-1}\sum_{i=1}^{N} z_i(x_i)^2$
8	2nd order moment of Gaussian surface	$m_2 = \frac{1}{L}\int_0^L \left(\frac{dz(x)}{dx} \right)^2 dx$	$m_2 = \frac{1}{N-2}\sum_{i=2}^{N-1} \left(\frac{z_{i+1} - z_{i-1}}{2h} \right)^2$
9	4th order moment of Gaussian surface	$m_4 = \frac{1}{L}\int_0^L \left(\frac{d^2 z(x)}{dx^2} \right)^2 dx$	$m_4 = \frac{1}{N-2}\sum_{i=2}^{N-1} \left(\frac{z_{i+1} - 2z_i + z_{i-1}}{h^2} \right)^2$

Table 3.2 Surface Profile Parameter Comparison

	m_0	m_2	m_4	Ra	Δ_a
Real Surface	0.141	0.0756	0.829	0.294	0.220
Cone	0.142	0.0751	0.935	0.272	0.219
Sphere	0.174	0.153	6.07	0.322	0.295
Pyramid	0.129	0.0936	5.16	0.293	0.216

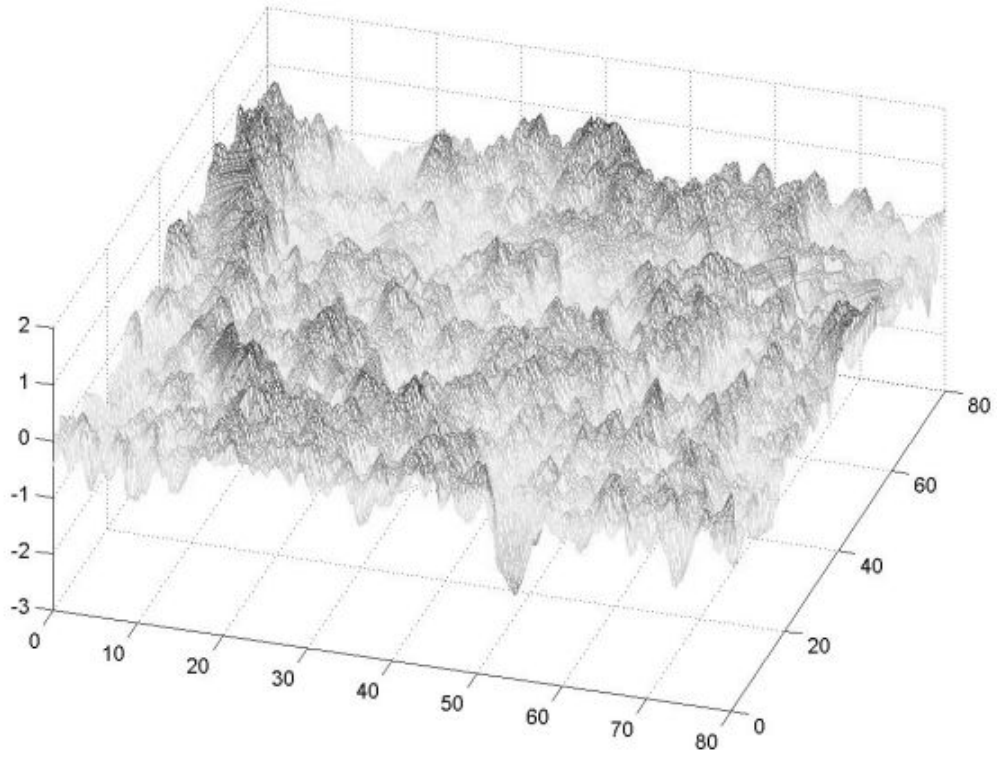

Figure 3.10 Real Surface Profile

3.3 Contact Mechanics of Cone

When a cone contacts with a workpiece which is assumed to induce rigid-plastic deformation (see Figure 3.11), prior research has found that the pressure along the tool-workpiece contacting surface is given by [54]:

$$p = 2k(1+\varphi) \tag{3.10}$$

where φ is function of cone angle $\alpha 1$:

$$\cos(2\alpha 1 - \varphi) = \frac{\cos\varphi}{1+\sin\varphi}. \tag{3.11}$$

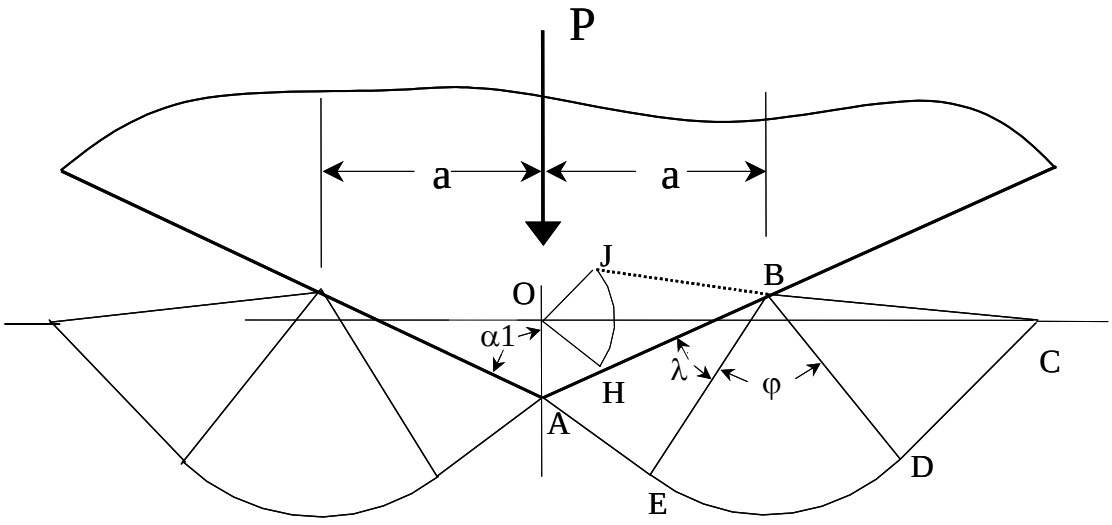

Figure 3.11 Cone Indentation Model (2-D View)

3.4 Real Contact Area Estimation

In their analysis of friction, Challen and Oxley [5] determined that the asperity angle of the tool surface is one of the dominant factors in determining the level of the friction produced. In the tool workpiece contact region, however, only a part of the area takes part in the contact (see Figure 3.12). This area, which is referred to as the real contact area, A_r, is often much less than the total (apparent) area of contact between the tool and workpiece. It is the real contact area that is most closely related to the magnitude of the friction force. This poses a significant problem when analyzing friction because there are no documented methods for measuring the real contact area in cutting processes. The real contact area has been calculated using statistical [55] and numerical approaches [56,57], but these models are based on primarily elastic deformation. In an effort to improve the prediction of friction in metal cutting processes, the plastic deformation model, which is introduced in the previous section, is proposed in this work to calculate the real contact area in a metal cutting process.

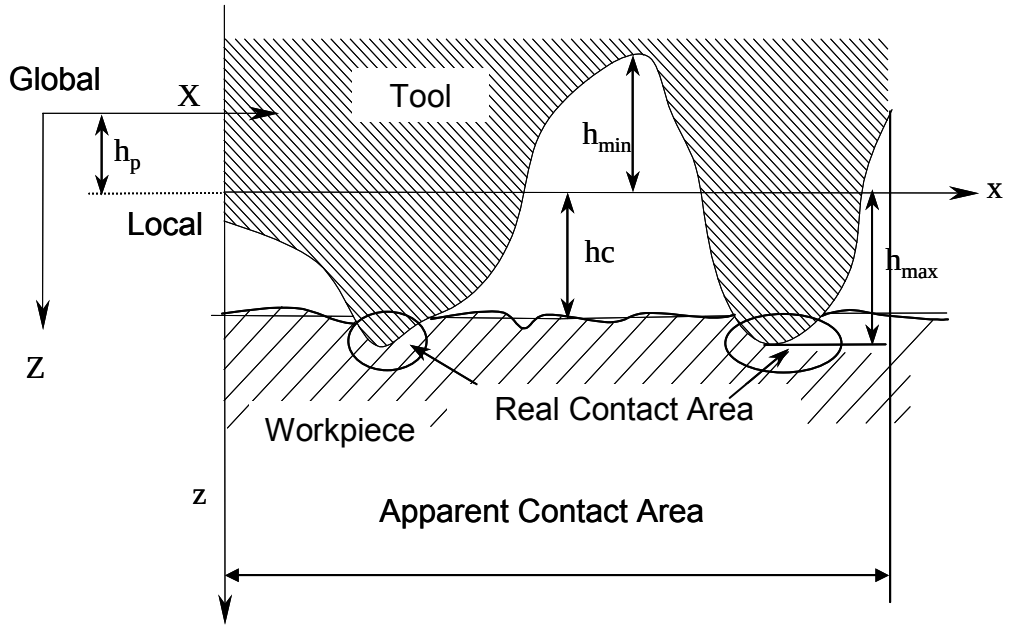

Figure 3.12 Illustration of Rough Surface Contact

To calculate the ratio of the real contact area with the apparent contact area, the measured area of the hard surface (tool) is divided into small areas (elements) that can be analyzed individually. Each element is looked as being located on a cone with known parameters. In order to estimate the real contact area between the tool and the workpiece, the load carried by each of the smaller areas of contact must be calculated. The summation of the loads on each of these areas will then be equivalent to the total load applied to the cutting tool:

$$F_T = \sum_{i=1}^{n} F_i \quad \text{(n= total number of elements)} \qquad (3.12)$$

As will be discussed in section 5.3, the total force during a material cutting process, F_T, can be experimentally determined for a cutting operation. As shown in Figure 3.13, to

evaluate the real area of contact for a given tool-workpiece combination, the tool surface profiles must first be obtained and simulated by cones. By estimating a penetration depth, the contact forces in each cone can be calculated using equation (3.10) and (3.11). The accuracy of penetration depth can be determined by summing forces of individual elements and comparing them to the applied (known) force. In the calculation, if the profile for calculation is not the entire apparent contact area, the added load on the tool must be averaged onto the measured surface area. By iterating on the penetration depth using the total force as a convergence criterion, an accurate value of the penetration depth can be obtained. Once the penetration depth is known, the real contact area can be determined by summing areas of the asperities whose z dimension values are greater than the penetration depth.

From Equation (3.10), The critical indentation depth is closely related to the material properties of the soft material. At elevated temperatures, the properties will change remarkably. It will then significantly influence the indentation depth as well as the real contact area. Change of the real contact area brings the change of the average slope of the asperities. Consequently, the friction will vary at elevated temperatures.

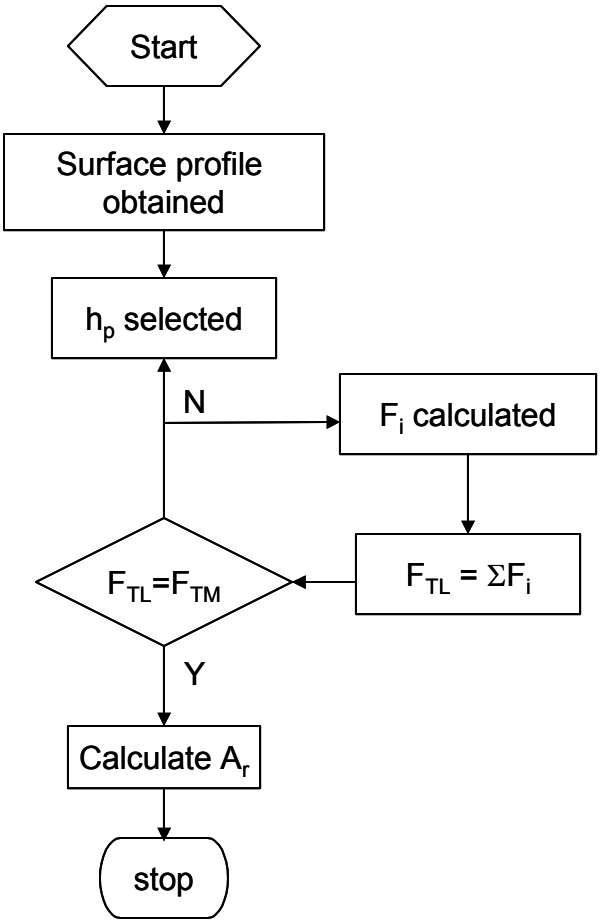

Figure 3.13 Procedures of A_r Calculation

4.0 EXPERIMENTATION

4.1 General Introduction

As discussed in Chapter 3.0, friction is influenced by the workpiece properties and the real contact area between the tool and the workpiece. To gain a better understanding of friction, experiments were conducted to study how the material properties and the coating of cutting tools influence the friction at elevated temperatures. Friction tests were carried out at more than 90 different operating conditions to analyze the role of the coating materials and the workpiece material properties. These conditions included varying the temperature (22°C—400°C), the tool insert coating materials, and the workpiece materials. In the experiments, gray iron, ductile iron, titanium, 6061 Al, and 2024 Al were used for the workpiece material and commercial TCMT21.51 Al_2O_3, TiC/TiN, and TiN coated inserts were used for the cutting tools.

4.2 Friction Tests

4.2.1 Friction Test Apparatus

1. Tribometer. A Falex ISC-200PC was used to study friction between tools and workpieces. The system consisted of a tribometer (see Figure 4.1) and a computerized data acquisition unit. The top platform of the tribometer contained a rotating vertical shaft assembly [A] that held a thin cylindrical workpiece [B]. A tool holder assembly [C] was attached to a precision balanced lever arm [D]. This lever arm was used to apply a vertical load to the tool and to measure the friction force experienced during sliding

motion. The tool was normally loaded against the disk by attaching weights to the arm. A load cell (force gauge) [E] attached to the base of the arm was used to measure the friction force as the workpiece surface was turned at a known angular velocity. The friction coefficient (ratio of the tangential force and the normal load) and the force data could then be stored using the computerized data acquisition system.

2. Insulation Parts. In order to perform elevated temperature friction experiments, an insulation containment system was designed and attached to the workpiece holder. Depicted in Figure 4.1(b), the containment system was made of a commercial Super Firetemp X material. The thermal conductivity of this material is 0.094 W/m·K at the temperature of 93°C and 0.115 W/m·K at the temperature of 427°C. As shown in the figure, the insulation container consisted of three parts. The first part was a cylindrical insulation chamber that was placed around the entire tool holder and workpiece. The insulation chamber was fixed to the bottom of the workpiece holder of the tribometer. The second component of the insulation container was the workpiece holder. The insulated holder was designed so that the workpiece would be held into place as the holder was rotated at the desired velocity. The final component of the insulated assembly, the top cover, was placed over top of the insulated assembly so that heat did not escape into the atmosphere. There was a small hole in the top cover to allow insertion of the cutting tool during experiments.

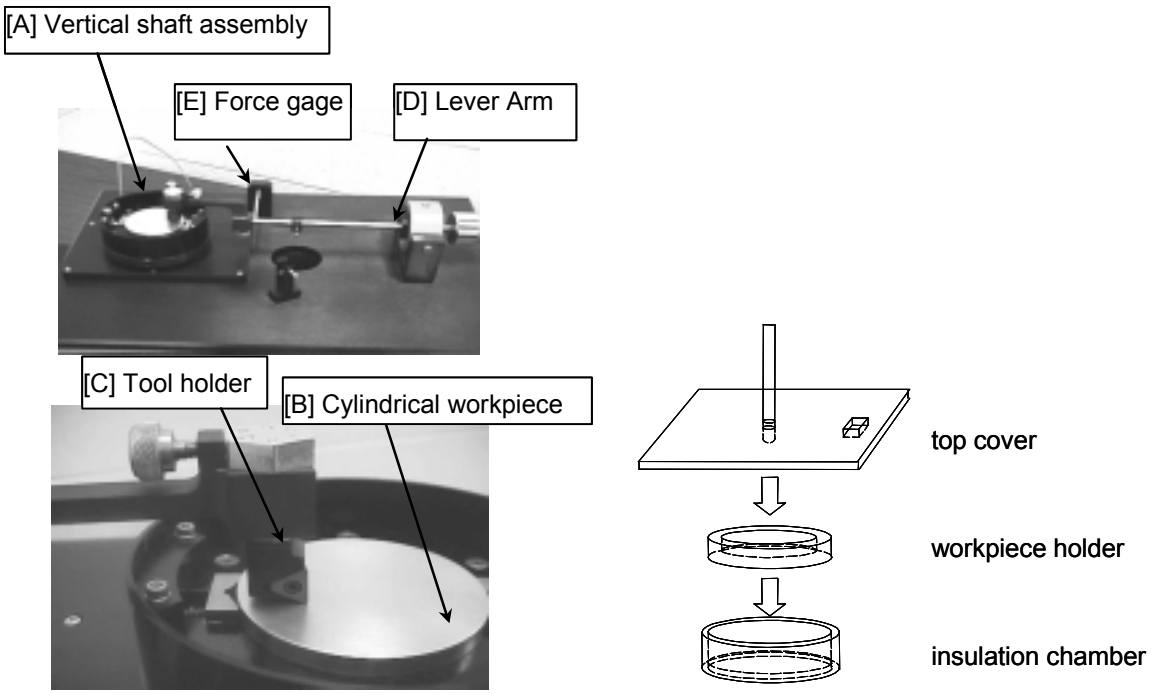

(a) Tribometer (b) Insulation Parts

Figure 4.1 Friction Measuring System

3. Device Control and Data Acquiring Program. The operational parameters can be set on the panel of the tribometer. Two parameters that must be carefully checked and set before each running are the workpiece angular velocity (ω) and the tool offset to the workpiece-rotating center (r). The sliding velocity (v) of the cutting tool against the workpiece is:

$$v = 2\pi r\omega \qquad (4.1)$$

In the tests, v=2500 mm/min was used.

The operating program of the tribometer includes three important function modules: parameter setting & device controlling, data displaying & saving, and data processing & exporting. Each module is introduced below:

(1) Parameter setting & device controlling. An advantage of the control program is that the sliding distance can be set from the control menu. The tribometer can be started and stopped from the program manually. However, it can also stop running automatically by setting stop criteria. There are three criteria to stop the test: moving distance, rotating cycles, and running time. In this test, the moving distance of 500mm is used in the tests as the stop criterion.

(2) Data displaying & saving. In each experiment, the friction value is plotted dynamically as a function of time. This function provides the possibility of checking the quality of tests. Sometimes, there will be unneeded disturbance during the tests because of unknown factors. With the dynamic display, the test can be stopped and

repeated whenever the abnormal appearance is observed. The data can also be saved as a file which can be loaded into the system for processing.

(3) Data processing & exporting. The program also provides the data processing ability, such as the mean value analysis and the band analysis. The time sequential friction coefficient data (see Figure 4.2) can be exported into a plain text file to be processed by other programs.

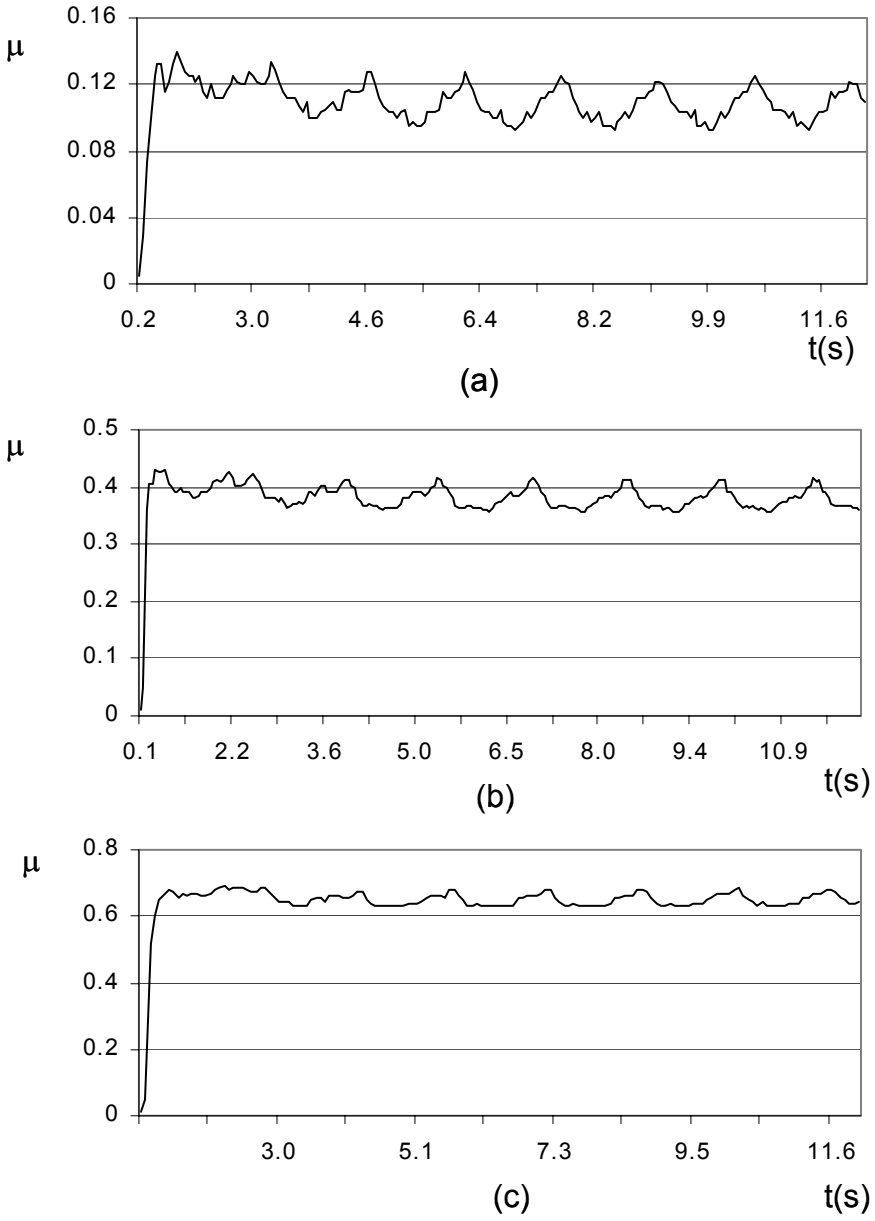

Figure 4.2 Friction Coefficient as a Function of Time

4.2.2 Cutting Tools

Commercial inserts were used for the tests. The inserts are identified as TCMT21.51. In the ISO identification system, the first 'T' indicates the shape of insert is triangle. 'C' means the relief angle of insert is 7°. 'M' is the tolerance indicator and the second 'T' provides the information of the lock hole. The number after letters gives the information of the insert dimension. Inserts of different coatings were chosen for the tests. The detail information of the tools is listed in Table 4.1.

Table 4.1 Cutting Tools Used in the Experiment

Inserts	Description	Side Length	Thickness	Shape	Coating
1	TCMT21.51	1/4"	1.5/16"	Triangle	AL_2O_3
2	TCMT21.51	1/4"	1.5/16"	Triangle	TIN/TiC
3	TCMT21.51	1/4"	1.5/16"	Triangle	TiN

4.2.3 Workpieces

The workpieces made from gray iron, ductile iron, titanium, Al 2024, and Al 6061 were used respectively. The workpieces were designed to the specific shape so that it can be

fit in the insulation holder. The surfaces of the workpiece were carefully prepared. On the automatic grinding machine, workpieces were grounded by grade 200, 400, and 600 grinding paper step by step. After being (wet) ground and dried, workpieces were gently polished using grade 600 paper manually to remove the hard localized oxide which was formed in the wet grinding processes.

4.2.4 Friction Test Procedure

Tests at various conditions were carried out. The tests were operated using the following procedures:

(1) Prepare for the tests. Turn on the furnace. Adjust the furnace temperature to designated temperature. Put the insulation chamber and the cover into the furnace. Hold the temperature for about four hours.

(2) Set the workpiece into the insulation chamber in the furnace, and leave the cover open. Hold for 30 minutes.

(3) Before running, change the tool insert, and adjust the rotating velocity ω and contacting radius r.

(4) Set the stop criterion of the control program.

(5) Cover the insulation chamber and take out the insulation set from the furnace. Put the sets into the workpiece holder quickly.

(6) Run the test.

(7) Save the data and read the friction value.

(8) Repeat step (2) to step (7).

4.3 Surface Profile Tests

In addition to the friction coefficient experiments, the surface profiles of the tool inserts (see Figure 4.3) were measured using Atomic Force Microscopy (AFM) before each set of friction tests. Detail description of test is list in Table 4.2. Profile parameters are listed in Table 4.3. Profile data was imported directly into Matlab so that the average asperity angles could be calculated.

Table 4.2 Surface Profile Test Description

Description	Value
Equipment	Nanoscope III
Mode	Tapping
Tip Material	Silicon
Tip Radius	10nm
Amplitude Set point	2.0V
Test Area	$80\times80\mu m^2$

Table 4.3 Surface Profile Parameters of Inserts

Insert coating	Rp(μm)	Rv(μm)	Ra(μm)
Al_2O_3	1.22	-2.61	2.92
TiC/TiN	1.39	-0.74	2.40
TiN	2.33	-1.73	2.60

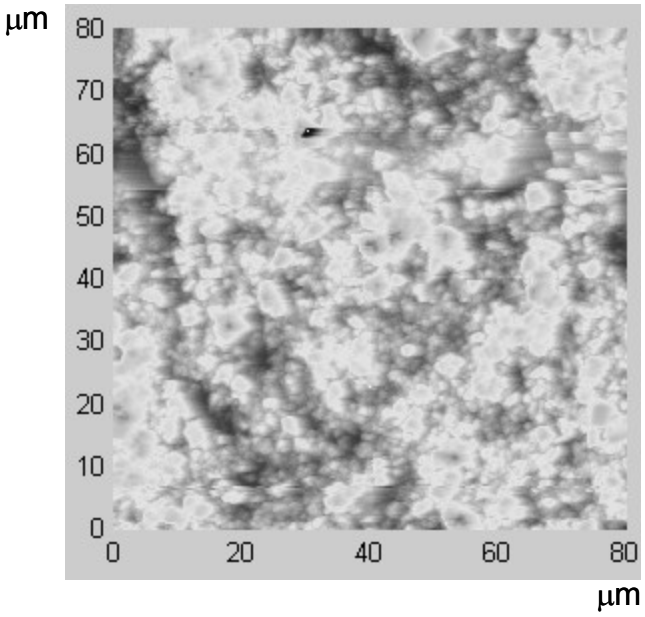

(a) Al_2O_3 Coating

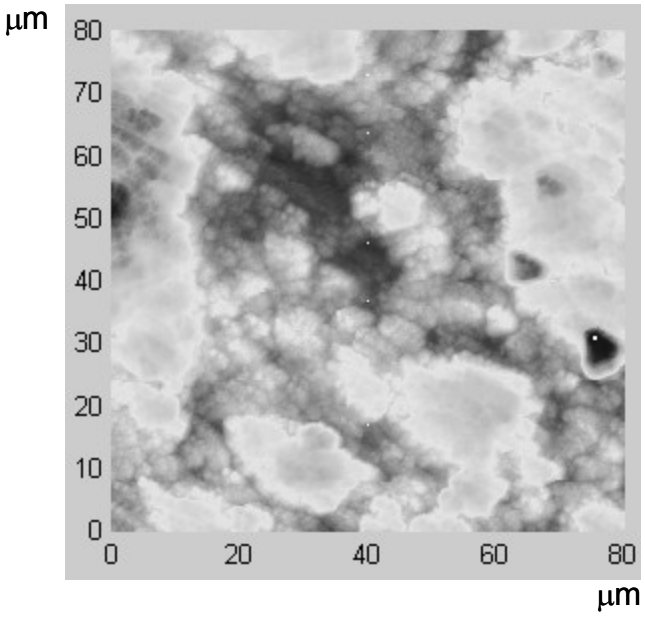

(b) TiC/TiN Coating

Figure 4.3 AFM Image of Coated Tool Surfaces

“Figure 4.3 continued”

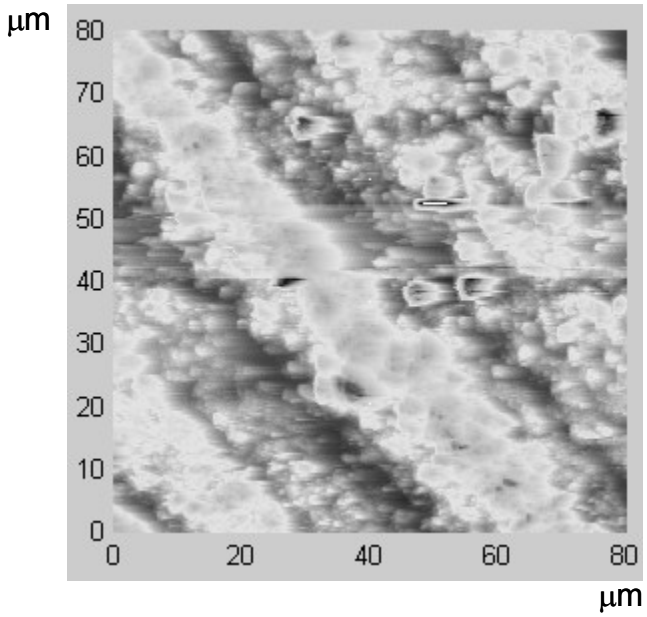

(c) TiN Coating

Figure 4.3 AFM Image of Coated Tool Surfaces

4.4 Apparent Contact Area Tests

The apparent area of contact was measured for each operating condition using standard indentation techniques. After carefully applying a thin layer of viscous oil onto the tip of the tool insert, experiments were interrupted after a very short time duration. Since the viscous oil adheres onto the workpiece, the apparent area of contact was determined by measuring the oil spot on the workpiece under low magnification (50×) microscope.

5.0 RESULTS AND DISCUSSION

5.1 Friction Test Results

Utilizing the friction testing apparatus, friction coefficient data was generated as a function of temperature, insert coating material, and workpiece material. The results of these tests are graphically depicted in Figure 5.1. Examining the curves for each workpiece material, several distinct trends are found. The first notable tendency is that for a given workpiece and coating material, the friction coefficient significantly increases with temperature. As shown in the figure, however, the relative change in the friction coefficient with temperature distinctly varies with the type of the workpiece material. For Al 2024 T4 and Al 6061 T6 (Figure 5.1d and Figure 5.1e), for example, the friction coefficients sharply increase (500%) with temperature. This is in contrast to gray iron, ductile iron, and titanium where a less significant increase in the friction is found over the same temperature range.

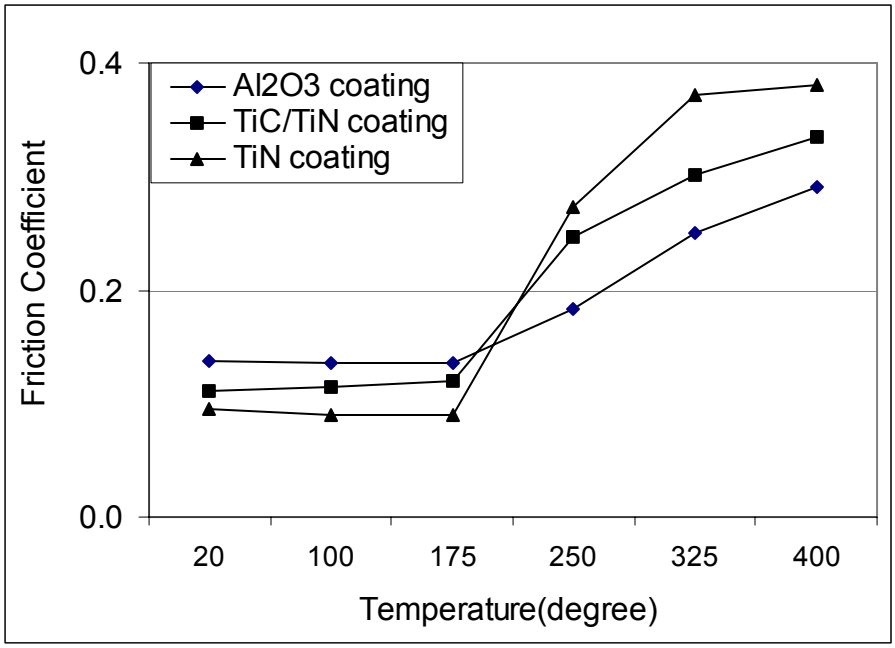

(a) Workpiece Material: Ductile Iron

Figure 5.1 Friction Coefficients vs. Temperatures

"Figure 5.1 continued"

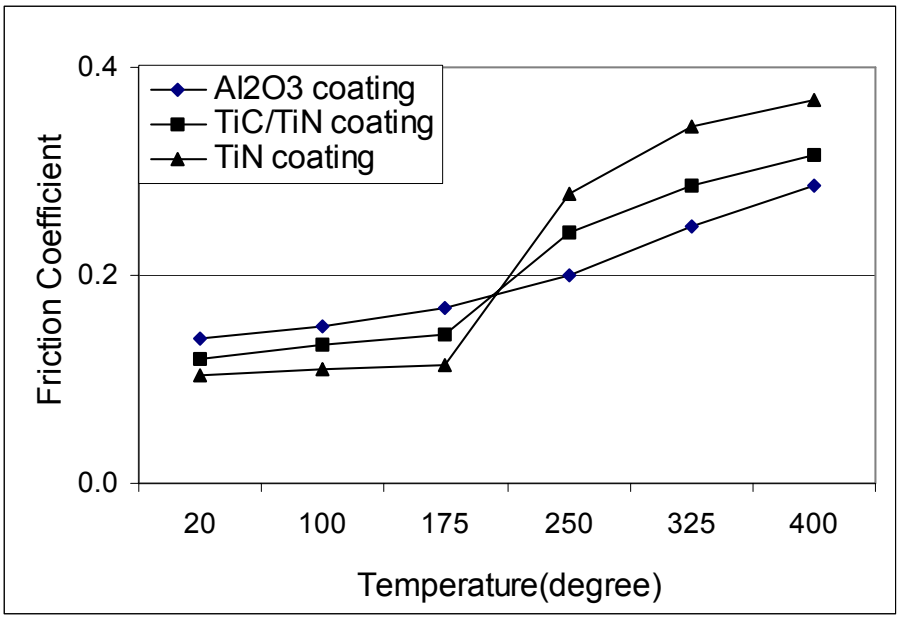

(b) Workpiece Material: Gray Iron

Figure 5.1 Friction Coefficients vs. Temperatures

"Figure 5.1 continued"

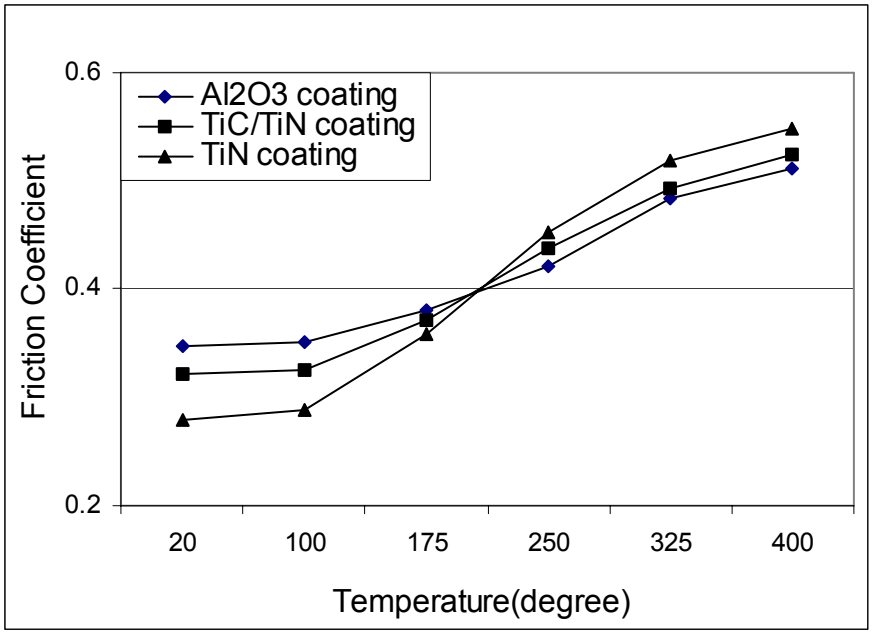

(c) Workpiece Material: Ti

Figure 5.1 Friction Coefficients vs. Temperatures

“Figure 5.1 continued”

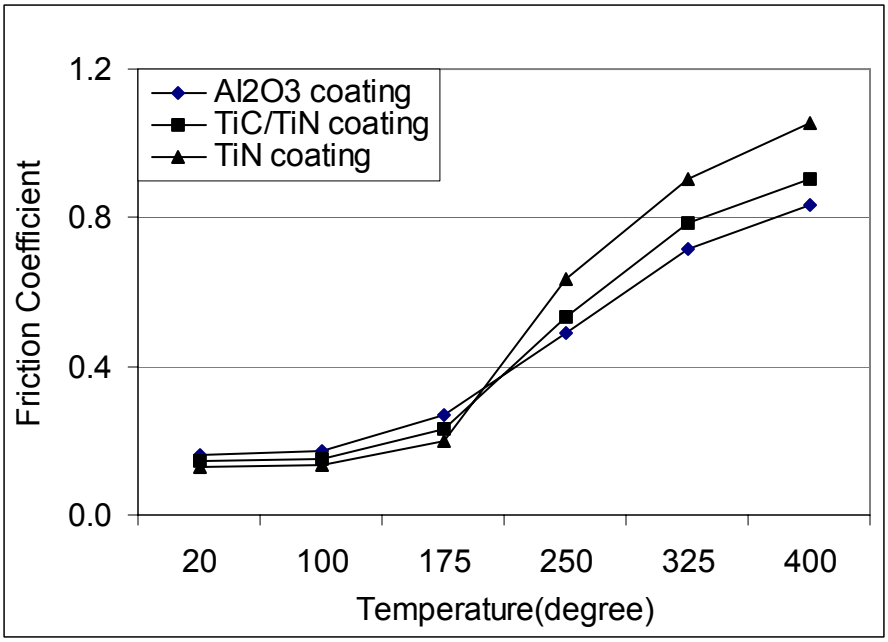

(d) Workpiece Material: Al 2024 T4

Figure 5.1 Friction Coefficients vs. Temperatures

"Figure 5.1 continued"

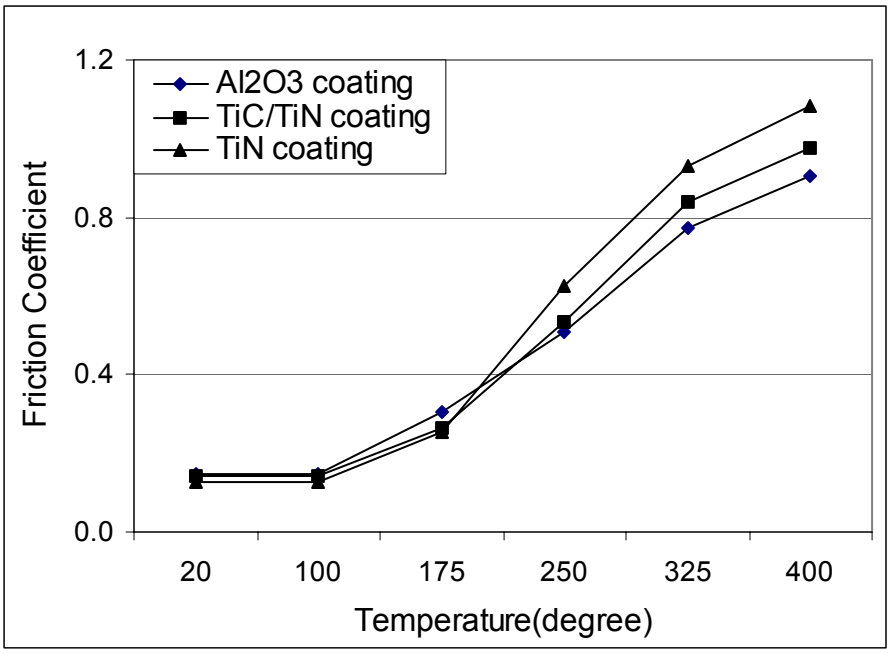

(e) Workpiece Material: Al 6061 T6

Figure 5.1 Friction Coefficients vs. Temperatures

A second important trend is the relative variation of the friction coefficient with coating material. For each workpiece material, the Al_2O_3 coating insert is found to have the largest friction coefficient at room temperature while TiN has the smallest. As the temperature increases, however, the relative increase in the friction coefficient is significantly larger for the TiN coating than for the Al_2O_3 coating. In fact, between 175^{o}C and 250^{o}C, there is a transition in the friction coefficient values and the friction of the TiN coating becomes greater than that of both Al_2O_3 and TiC/TiN. The coating materials maintain this order until the highest temperature examined of 400^{o}C. The TiC/TiN coating maintains a friction coefficient level between the TiN and Al_2O_3 coatings regardless of the temperature. These tendencies for the coating materials are consistent with the published reports in the literature.

5.2 Friction vs. Workpiece Properties

The tendency that the friction increases with the temperature can be explained using the premise established by Challen & Oxley [5]. As being expressed in Equations 2.10-2.11, there are two dominant factors which influence the friction between the cutting tool and workpiece: the roughness parameter, α, and the shear flow stress parameter, *f*.

We will attempt to explain the trends found in Figure 5.1 based on the roughness and shear flow stress parameters introduced by Challen & Oxley. Let us first consider the influence of the shear flow stress parameter, *f*, in our experiments. In Equation (2.12), *f*

is defined by $f = \tau / k$, where the workpiece flow strength is given by the empirical relationship [20]:

$$k = 221.3\gamma^{0.128} \tag{5.1}$$

In Equation (5.1), γ is the shear strain of the workpiece. From the definition, the shear strain is defined as:

$$\gamma = \frac{1}{2}\left(\frac{\partial u_x}{\partial y} + \frac{\partial v_y}{\partial x} \right), \tag{5.2}$$

where u_x and v_y are displacements of the defined element along the x and y axes respectively. These displacements can be expressed by the displacements (u and v) or velocities along the slip-lines shown in Figure 2.2:

$$\begin{cases} u_x = u\cos\psi - v\sin\psi \\ v_y = u\sin\psi + v\cos\psi \end{cases} \tag{5.3}$$

If the coordinate system is constructed in such a manner that slip-line I is on the x axis and slip-line II is on the y axis, the shear strain in Equation (5.2) can be expressed as:

$$\gamma = \frac{1}{2}\left(\frac{\partial u}{\partial y} + \frac{\partial v}{\partial x} \right). \tag{5.4}$$

From Equation (5.4) the velocity discontinuity[20] (see Figure 2.4 (b)) in the deformed field can be expressed as:

$$\gamma = \frac{v^*_{AB}}{v^n_{AB}} + \frac{v^*_{BE}}{v^n_{BE}} + \frac{v^*_{CD}}{v^n_{CD}}. \tag{5.5}$$

In Equation (5.5), the v^*'s are the velocity discontinuities along the boundary of the slip-line field, and the $v^{n'}$s are the normal components of the corresponding v^*'s. From the hodograph in Figure 2.4(b), the velocity discontinuity relationship is expressed by:

$$\mathrm{T1} = \frac{v_{AB}^{*}}{v_{AB}^{n}} = \frac{2\sin(\eta)}{\cos(\eta) - \sin(\eta)} \qquad (5.6)$$

$$\mathrm{T2} = \frac{v_{CD}^{*}}{v_{CD}^{n}} = \frac{\sin(\alpha)}{\sin(\phi)\sin(\alpha + \phi)} \qquad (5.7)$$

$$\mathrm{T3} = \frac{v_{BE}^{*}}{v_{BE}^{n}} = \frac{2\sin(\alpha + \eta)}{\cos(\alpha + \eta) + \cos(\frac{\pi}{4} - \alpha - \phi)} \qquad (5.8)$$

In Equations (5.6) - (5.8), the angles η, and ϕ are functions of $\alpha, \tau,$ and *k* (Equation (2.9)):

$$k = \Phi(\alpha, \tau, k) = 221.3(\mathrm{T1} + \mathrm{T2} + \mathrm{T3})^{0.128}. \qquad (5.9)$$

The value of τ can be obtained numerically by solving the nonlinear equation

$$\Psi(\alpha, \tau, k) = k - \Phi(\alpha, \tau, k) = 0. \qquad (5.10)$$

In Equation (5.10), τ can be determined using the secant method for a given roughness, α, and shear flow stress, *k*. Consequently, the friction coefficient can be directly obtained using Equation (2.12), as shown in Figure 5.2. From Figure 5.2, the friction coefficient is found to decrease as the shear flow stress of the workpiece material increases.

In order to connect the friction coefficient with workpiece material, we can examine the shear flow stress of the workpiece as a function of temperature. Using the Von Mises' yield criterion, the shear flow stress, *k*, is related to the yield stress, *Y*, by:

$$\sqrt{3}k = Y, \qquad (5.11)$$

From Equation (5.11) and Figure 5.2, the friction coefficient will decrease as the yield stress of the workpiece material increases. Variation of the yield stress with temperature

for the five materials (see Figure 5.3) studied has been discussed in Section 3.1. As mentioned early, the yield stress values of Al 2024 and Al6061 sharply decrease between the room temperature and 400°C, while the yield stress of titanium, gray iron, and ductile iron show a less substantial decrease in the yield stress over the same temperature range. Hence, comparing Figure 3.5 and Figure 5.1, it is clear that as predicted by Challen & Oxley, the friction coefficient in material cutting processes depends on the magnitude of the workpiece flow stress, which is ultimately a function of cutting temperature.

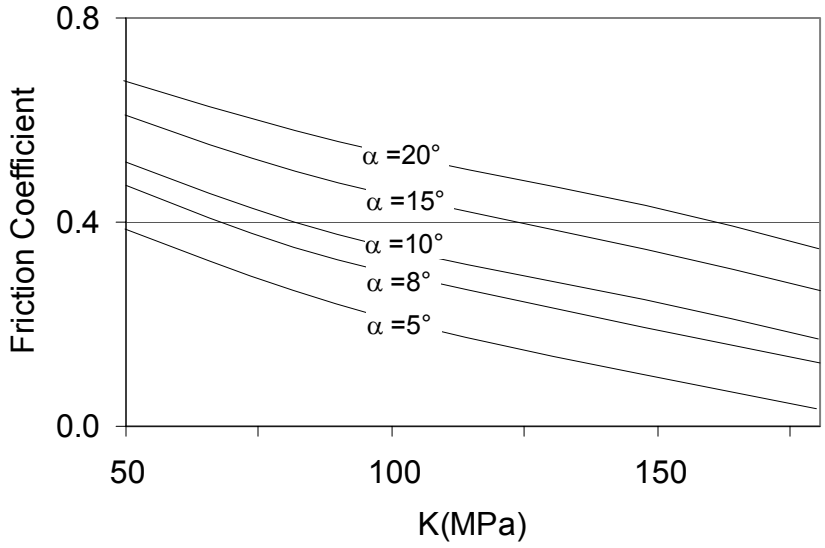

Figure 5.2 Friction Coefficient Variation with Shear Flow Stress

5.3 Friction vs. Tool Surface Asperity Angles

Another important aspect of the investigation is to analyze the role of coatings in material cutting processes from a fundamental perspective. For the purpose of obtaining a better understanding of the trends in Figure 5.1, the asperity interaction along the tool-workpiece interface was investigated for the operating conditions for which friction tests were performed. This was accomplished using the procedure outline in Section 3.3.

During contact between the cutting tool and the workpiece, the critical boundary height of the real contact area, z_p, can be calculated from the geometric values provide from the AFM surface profile and the procedure given in Section 3.3 (see Figure 3.13). Once z_p is obtained for a given operating condition, the slope of the real contact area can be calculated. Using z_p and the measured surface profiles, the real contact area for each tool coating material can be plotted for any temperature and workpiece material.

Although similar trends were found for all of the workpiece materials, the procedure for determining the asperity interaction and the real contact area will be demonstrated for Al 6061 T6 (see Table 5.1 for material properties). Figure 5.3 shows the real contact area as well as the average slope angle for each of the coating materials from room temperature to 400 ^{o}C. The comparison of the real contact area from room temperature to 400 ^{o}C for Al_2O_3 is shown in Figure 5.4. As shown in the figures, the real area of contact and the average slope angle significantly increase with temperature for each

coating material. This is due to the fact that the workpiece material becomes significantly more compliant at elevated temperatures, and therefore the tool will more readily penetrate and plastically deform the workpiece surface. Such an increase in the real area of contact as well as in the average slope angle also explains the increase in the friction coefficient with temperature that is shown in Figure 5.1. A similar pattern between Figure 5.1 and Figure 5.3 (b) is that sharp change occurs between 175 ^{o}C and 325 ^{o}C. For a higher real contact area, there is more asperity interaction between the tool and workpiece, which leads to higher friction coefficient values.

The trends for the friction variation with temperature with different coating materials can also be explained by examining the changes in the asperities (see Figure 5.3). The calculation indicates that there is variation of the real contact area between the coated surfaces. From Figure 5.3(b), the slope difference between insert surfaces is clear. The slope values are directly related to the measured friction results. At the room temperature, TiN has the smallest average slope angle, which is corresponding to the smallest friction value at the room temperature. Likewise, at 400^{o}C, Al_2O_3 has the smallest slope angle and the real area of contact at 400^{o}C while TiN has the largest, which again follows the trends for the friction.

Further explanation of the results can be found from the distribution density of the surface profile. Surfaces are usually assumed to exhibit a Gaussian distribution. However, the real surface can't be distributed with such an idealized form. The spectral distribution function can be obtained directly from the magnitude of the z dimension for each point on the measured surface. When the distribution density functions of the

measured surface profile and the Gaussian distribution density functions are plotted, noticeable difference between the distribution densities is observed (see Figure 5.5). In Figure 5.5, the deviation of the Gaussian distribution is obtained from the average deviation value of three different coated surfaces. The overall deviation of the distribution functions and the local irregularity cause the difference of the average real contact slope.

Table 5.1 Mechanical Properties of Al6061-T6 at Elevated Temperatures

Temperature(°C)	Young's Modulus(Gpa)	Yield Strength (Mpa)
22	72	275
100	69	230
175	65	142
250	59	45
325	51	18
400	41	12

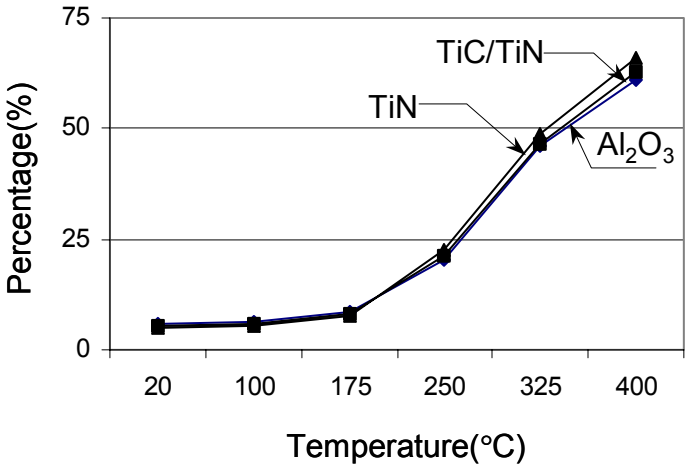

(a) Ar/Aa vs. temperature

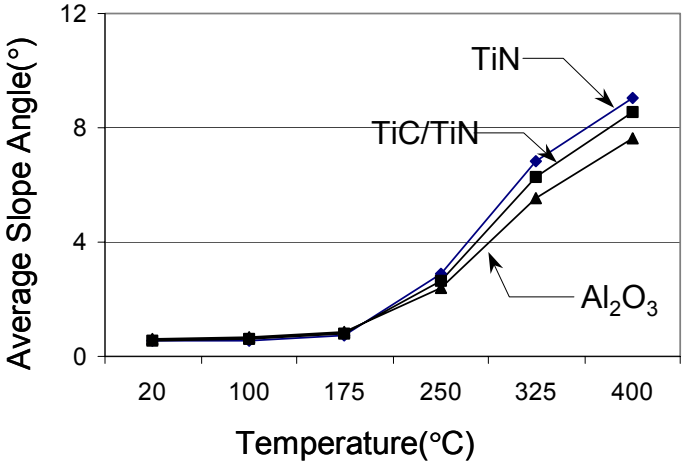

(b) Slope angle vs. temperature

Figure 5.3 Real Contact Area and Slope Angle Change with Temperature

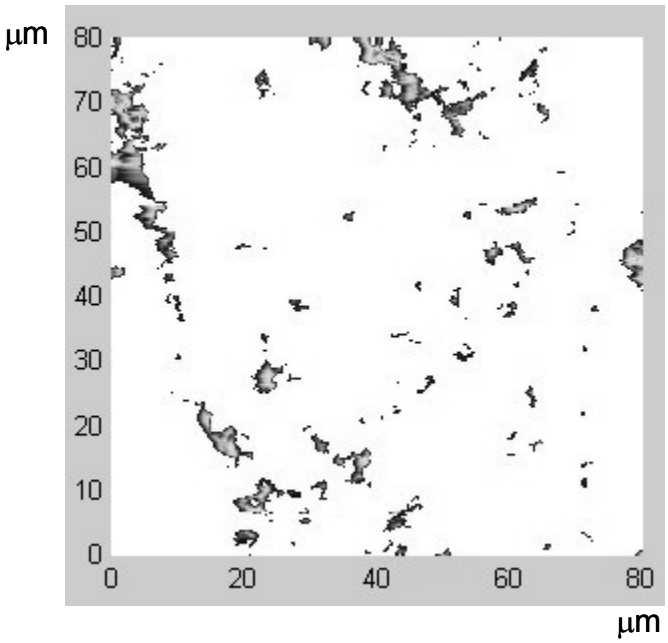

(a) Workpiece 22°C

Figure 5.4 Real Contact Area on Al_2O_3 Coated Insert Surface

“Figure 5.4 continued”

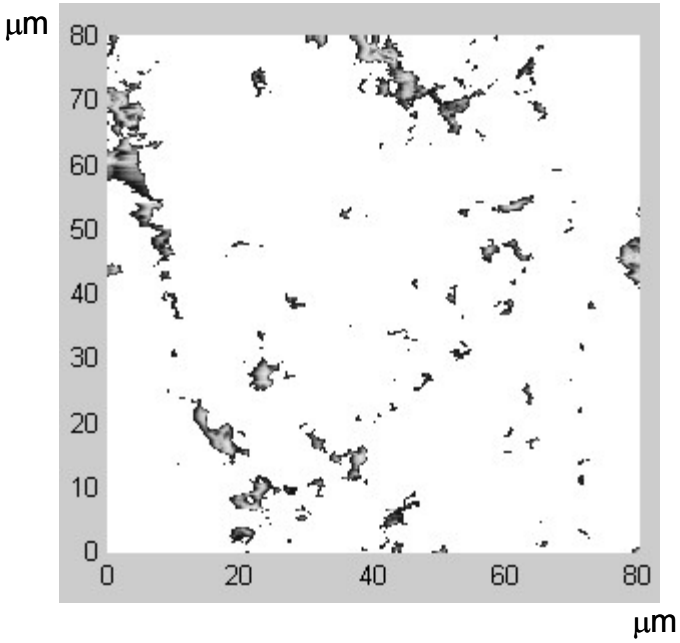

(b) Workpiece 100°C

Figure 5.4 Real Contact Area on Al2O3 Coated Insert Surface

“Figure 5.4 continued”

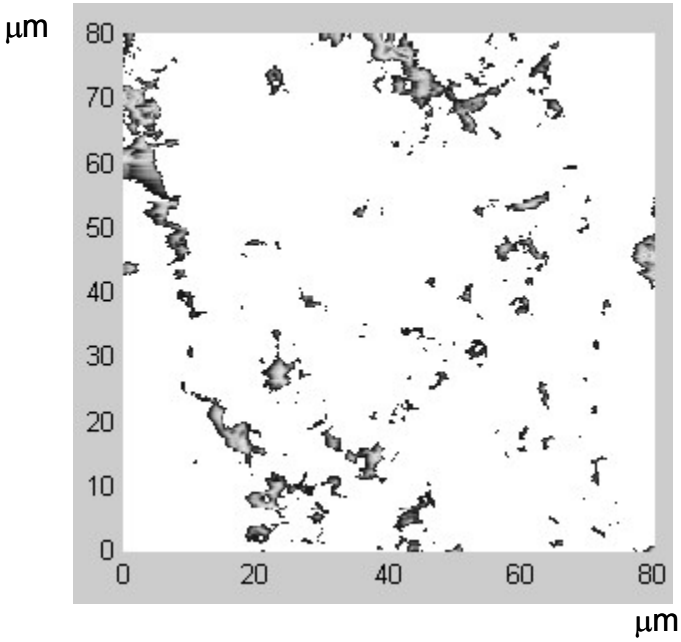

(c) Workpiece 175°C

Figure 5.4 Real Contact Area on Al2O3 Coated Insert Surface

“Figure 5.4 continued”

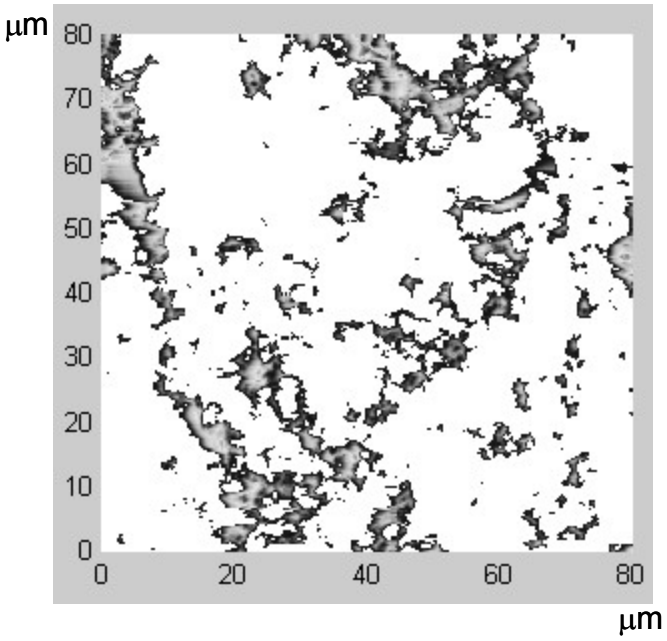

(d) Workpiece 250°C

Figure 5.4 Real Contact Area on Al2O3 Coated Insert Surface

“Figure 5.4 continued”

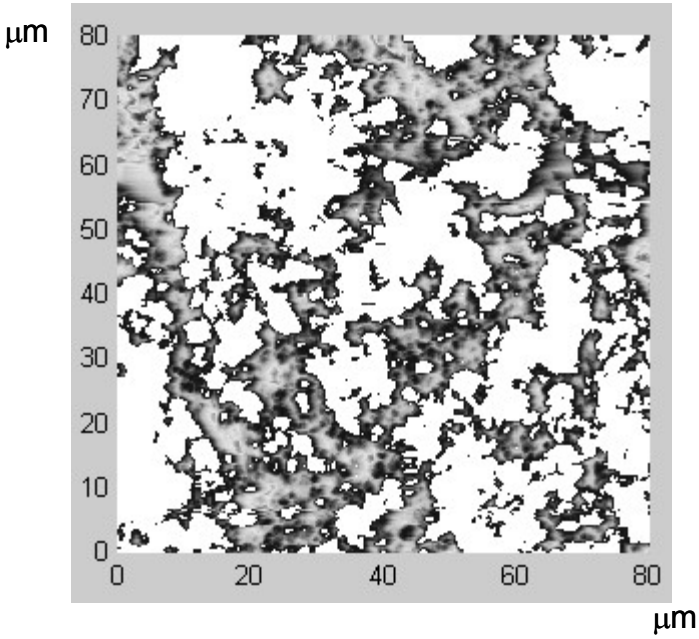

(e) Workpiece 325°C

Figure 5.4 Real Contact Area on Al2O3 Coated Insert Surface

“Figure 5.4 continued”

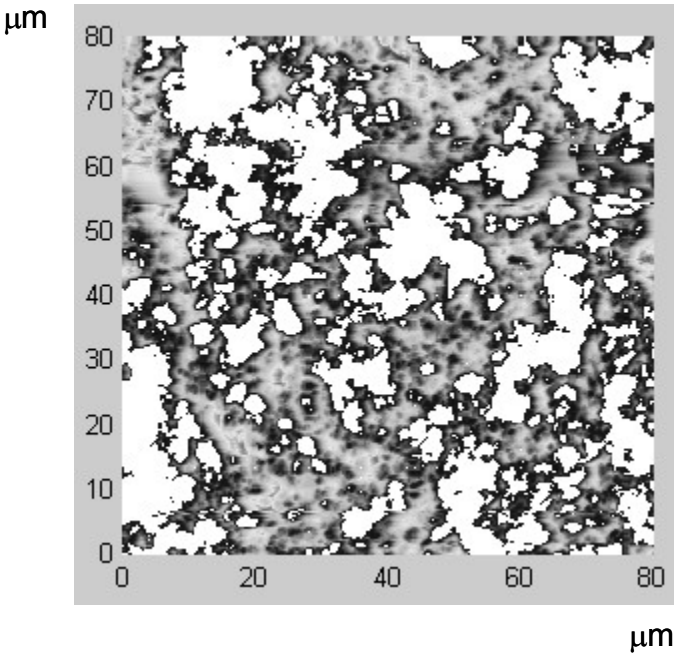

(f) Workpiece 400°C

Figure 5.4 Real Contact Area on Al2O3 Coated Insert Surface

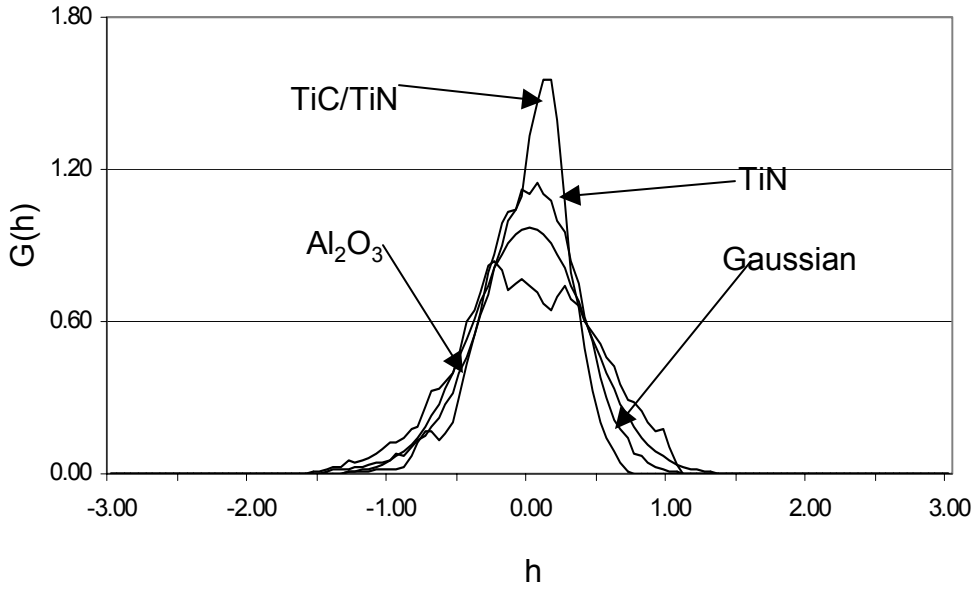

Figure 5.5 Distribution Density Functions

5.4 Development of Empirical Friction Model

Inspired by Equation (2.14), it was desired to develop a direct relationship between the shear stress along the cutting interface, τ, and the flow strength of the workpiece material, k. As being discussed in previous section and demonstrated in the experiments, material properties of the workpiece material have a substantial influence on the friction coefficient in material cutting processes. The yield strength of workpiece material is directly related to the shear flow stress. From the analysis of the real contact area (Equation 3.10), the yield strength of workpiece material dominates the ratio of the real contact area. Plotting A_r/A_a as a function of the yield strength of the workpiece

material directly, yield strength of workpiece material is found to have significant influence on A_r/A_a (Figure 5.6).

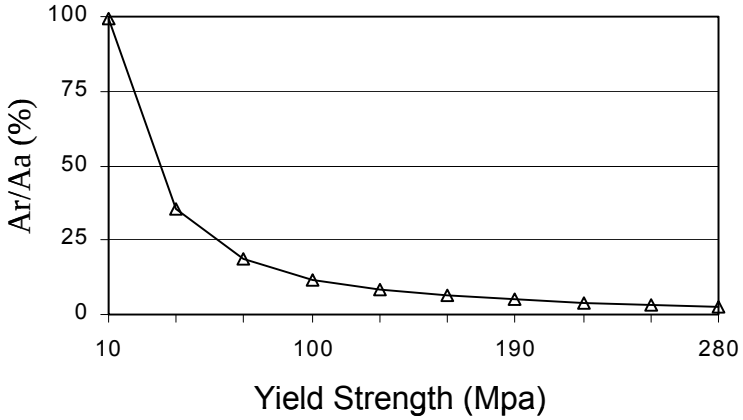

Figure 5.6 Material Properties vs. A_r/A_a

For the purpose of predicting the friction in material cutting processes, an empirical relationship was generated in the form:

$$\mu = \zeta + \nu e^{(k(t))/100} \qquad (5.12a)$$

or, more directly,

$$\mu = \zeta + \nu e^{\left(\frac{Y(t)}{\sqrt{3}}\right)/100} \qquad (5.12b)$$

where ζ and v are the friction constants which vary with the material, $k(t)$ and $Y(t)$ are the shear flow stress and the yield strength of the workpiece material at a given temperature respectively. Friction coefficients can then be predicted as a function of temperature using Equation (5.12) and the yield strength values in Figure 3.5. The form of Equation (5.12b) was established by curve fitting the experimental friction data shown in Figure 5.1. The material friction constants ζ and v that best fit the experimental data are given in Table 5.2. Figure 5.7 shows a comparison between the experimental and empirically predicted friction coefficient values for Ti, Al2024 T4, and Al6061 T6. From the figure, the predicted friction coefficients match favorably with the experimental data for each material. The empirical relationships (5.12a) and (5.12b) can be applied directly into a finite element analysis code for material cutting processes.

Table 5.2 Coefficients for Different Materials

Material	ζ	v
Al6061	1.22	-0.23
Al2024	1.21	-0.24
Ti	0.085	-0.094
Gray Iron	-1.34	0.37
Ductile Iron	0.80	-0.12

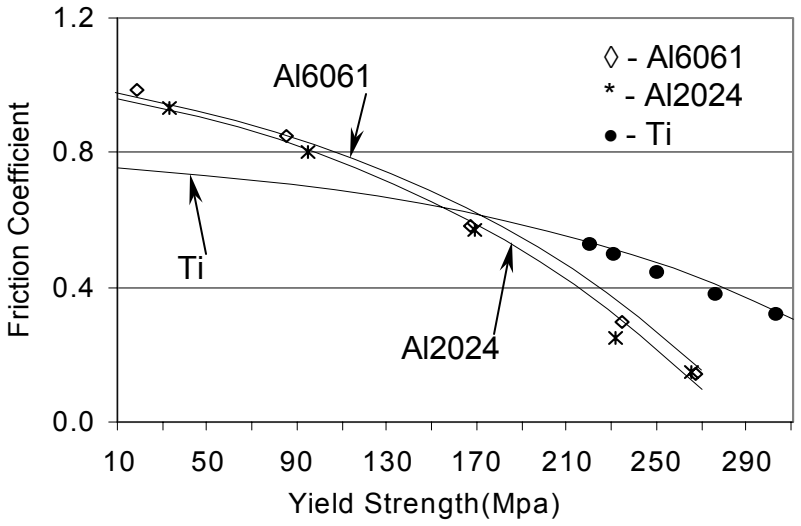

Figure 5.7 Relationship between the Yield Strength and the Friction Coefficient

It is noticed that Kim and Sin [20] deduced a similar expression for the friction coefficient in the form:

$$\mu = \lambda e^{-\lambda \frac{\sigma_n}{k}} . \qquad (5.13)$$

Comparing Equations (5.12a-b) with Equation (5.13), the advantage of Equations (5.12a-b) is that the normal stress σ_n , which is difficult to measure, doesn't have to be known a prior.

6.0 CONCLUSIONS

In this work friction-influence factors have been investigated at elevated temperatures for metal cutting processes. The material microstructure at the elevated temperature and the surface profiles of the cutting tool have been analyzed. An elastic-plastic model has been built to estimate the real contact area. By calculating the average slope angle of the surface profile asperities, it has been found that there is significant change of the slope angle. Experimental technique was also introduced to characterize the friction along the tool/workpiece interface in a metal cutting operation. By performing experiments at more than 90 different operating conditions, the influence of coating material and operating temperature was determined by analyzing the asperity interaction. The following is a summary of the findings obtained from the deductions and experiments:

1. The friction between the cutting tool and workpiece was found to increase with operating temperature. The increase was attributed to (1) changes in the mechanical properties of the workpiece material which are brought by the microstructure change at elevated temperatures and (2) the increase in the asperity interaction at higher temperature.

2. The friction coefficient in the material cutting process investigated has been found to be directly related to the real area of contact between the cutting tool and the workpiece. Change of the real contact area will influence the equivalent

average asperity slope angle of the cutting tool surface profile. According to Challen and Oxley's friction model, the friction will change in turn.

3. Tool coating material had a significant influence on the friction in the process studied. Al_2O_3 was found to perform best at higher temperatures while TiN performed better at lower temperatures. TiC/TiN coatings had a more consistent performance with respect to friction for the range of temperature studied.

4. Based on the analysis and the experimental results, an empirical relationship was generated for the friction coefficient. This relationship can be directly applied to improve the numerical accuracy in the finite element modeling of material cutting processes.

BIBLIOGRAPHY

BIBLIOGRAPHY

1. Merchant, M.E., "Mechanics of the Metal Cutting Process," J.Appl.Phys., Vol. 16 (1945), pp. 318-324.

2. Piispanen, V., "Theory of Formation of Metal Chips," J.Appl. Phys., Vol. 19 (1948), pp. 876-881.

3. Lee, E.H. and Shaffer, B.W., "The Theory of Plasticity Applied To a Problem of Machining," Trans. ASME J. Appl. Mech., Vol. 18 (1951), pp. 405-413.

4. Rowe, G.W. and Wolstencroft, F., "A Mechanical Approach To the Metallurgy of Metal Cutting," J.Inst. Metals, Vol. 98 (1970), pp. 33-41.

5. Challen, J. M. and Oxley, J. M., "An Explanation of the Different Regimes of Friction and Wear Using Asperity Deformation Models," Wear, Vol. 53 (1979), 228-243.

6. Oxley, P.L.B., "Rate of Strain Effect in Metal Cutting," J. Eng. Ind., Vol. 85 (1963), pp. 335-337.

7. Zienkiewicz, O.C., The Finite Element Method in Engineering Science (2^{nd} ed.; London 1971: McGraw Hill, 1971).

8. Kakino, Y., "Analysis of the Mechanism of Orthogonal Machining by the Finite Element Method," J. Japan Soc. Prec. Eng., Vol. 37(7) (1971), pp. 503-508.

9. Shirakashi, T. and Usui, E., "Simulation Analysis of Orthogonal Metal Cutting Process," J. Japan Soc. Prec. Egn., Vol. 42(5) (1976), pp. 340-345.

10. Shih, A.J., "Finite Element Simulation of Orthogonal Metal Cutting," ASME Journal of Engineering for Industry, Vol. 117(1995), pp. 84-93.

11. Strenkowski, J.S. and Carrol III, J.T., "A Finite Element Model of Orthogonal Metal Cutting," Trans ASME J. Eng. Ind. Vol. 107 (1985), pp. 349-354.

12. Iwata, K., Osakada, K. and Terasaka, Y., "Process Modeling of Orthogonal Cutting by the Rigid-Plastic Finite Element Method," Trans ASME J.Eng. Mat. Tech., Vol. 106(1984), pp. 132-138.

13. Maekawa, K. and Maeda, M., "Simulation Analysis of Three-Dimensional Continuous Chip Formation Processes (1st report)-FEM Formulation and a Few Results," J. Japan Soc. Prec. Eng., Vol. 59(11) (1993), pp. 1827-1833.

14. Sasahara, H. and Shirakashi, T., "FEM Analysis on Three Dimensional Cutting-Analysis on Large Deformation Problem of Tool Entry," Int. J. Japan Soc. Prec. Eng., Vol. 28(2) (1994), pp. 123-128.

15. Bowden, F. P. and Tabor, D., "The Area of Contact between Stationary and between Moving Surfaces," Pro. R. Soc, Lond., Vol. A169 (1939) pp. 391-413.

16. Bowden, F.P. and Tabor, D., The Friction and Lubrication of Solids, Part II, (New York: Clarendon Press, 1964).

17. Green, P., "The Plastic Yielding of Metal Junctions Due to Combined Shear and Pressure," J. Mech. Phys. Solids, Vol. 2 (1954) pp. 197-211.

18. Green, P., "Friction between Unlubricated Metals: a Theoretical Analysis of the Junction Model," proc. R. Soc. Lond., Vol. A228(1955) pp. 191-204.

19. Black, J., Kopalinsky, E. M. and Oxley, P. L. B., "An Investigation of the Different Regimes of Deformation Which Can Occur when a Hard Wedge Slides over a Soft Surface: the Influence of Wedge Angle, Lubrication and Prior Plastic Working of the Surface," Wear, Vol. 123 (1988), pp. 97-114.

20. Challen, J. M. , McLean, L. J. , and Oxley, P. L. B., "Plastic Deformation of a Metal Surface in Sliding Contact with a Hard Wedge: Its Relation to Friction and Wear," Proc. R. Soc. Lond. Ser. A, Vol. 394 (1984), pp. 161-181.

21. Lovell, M. R. and Deng, Zhi, "Experimental Investigation of Sliding Friction between Hard and Deformable Surfaces with Application to Manufacturing Processes," Wear, Vol. 236(1999), pp. 117-127.

22. Torrance, J. and Galligan, G., "A Model of the Friction of a Smooth Hard Surface Sliding over a Softer One," Wear, Vol. 212(1997), pp. 213-220.

23. Bhattacharya, S. and Lovell, M. R., "Characterization of Friction in Machining: Evaluation of Asperity Deformation and Seizure-Based Models," Transactions of NAMRI, Vol. 25 (2000), pp. 107-112.

24. Trent, E.M., Metal Cutting, (London: Butterworths, 1977).

25. Trent, E.M., "Metal Cutting and the Tribology of Seizure: I Seizure in Metal Cutting," Wear, Vol. 128 (1988), pp. 29-45.

26. Boothroyd, G., Fundamentals of Metal Machining and Machine Tool (New York: McGraw-Hill, 1975).

27. Zorev, N. N., Metal Cutting Mechanics (Pergamon Press 1966).

28. Trent, E. M., Metal Cutting (2nd ed.; London: Butterworths, 1984).

29. Wallace, P. W. and Goothroyd, G., "Tool Forces and Tool Chip Friction in Orthogonal Machining," J. Mech. Engng. Sci., Vol. 6(1964), pp. 74-87.

30. Finnie, M.C. Shaw, "The Cutting Process in Metal Cutting," Transactions of ASME, Vol. 78(1956), pp. 1649-1657.

31. Usui, E. and Shirakashi, T., "Mechanics of Machining -- From 'Descriptive' to 'Predictive' Theory, On the Art of Cutting Metals - 75 Years Later," ASME PED., Vol. 7(1982), pp. 13-35.

32. Die, N.N., "Schneide Verdient das Geld, " Schneidstoffe- Indikatoren vielschichtiger Internationaler Entwicklungen, Fertigung, Landsberg, Vol. *2* (1991), pp. 12-15.

33. Wick, C., "Coatings Improve Tool Life, Increase Productivity," Manufacture Engineering, Vol. 97(1986), pp. 26-31.

34. Sandvik, C., Modern Metal Cutting (NJ: Sandvik Coroment, 1996).

35. Du, F., Lovell, M. R. and Wu, T. W., "Boundary Element Method Analysis of Temperature Fields in Coated Cutting Tools," International Journal of Solids and Structures, Vol. 38 (2001), pp. 4557-4570.

36. Sundgren, J.E., Birch, J., Hakansson, G., Hultman, L. and Helmersson, U., "Growth, structural characterization and properties of hard and wear-protective layered materials," Thin Solid Films, Vol. 193-194 (1990), pp. 818-831.

37. Vancoille, E., Celis, J. P. and Roos, J. R., "Tribological and Structural Characterization of a Physical Vapor Deposited TiC/Ti(CN)/TiN Multiplayer," Tribology International, Vol. 26(2) (1993), pp. 115-119.

38. Grzesik, W., "The Influence of Thin Hard Coatings on Frictional Behavior in the Orthogonal Cutting Process," Tribology International, Vol. 33(2000), pp. 131-140.

39. Lim, C.Y.H., Lim, S.C., and Lee, K.S., "The Performace of TiN-Coated High Speed Steel Tool Inserts in Turning," Tribology International, Vol. 32(1999), pp. 393-398.

40. Donnelly, N., McConnell, M., Dowling, D.P. and O'Mahony, J.D., "A Comparison between the Tribological and Mechanical Properties of TiN and TiCN," Material Science Forum, Vol. 325-326(2000), pp. 141-146.

41. Bull, S.J. and Jones, A.M., “Multilayer Coatings for Improved Performance,” Surface and Coatings Technology, Vol. 78(1996), pp. 173-184.

42. Proceedings of the CIRP International Workshop on Modeling of Machining Operations, 1988, “Modeling of Orthogonal Machining Processes for Variable Tool-Chip Interfacial Friction Using Explicit Dynamic Finite Element Methods, by Lovell, M.R., Bhattacharya, S., and Zeng, R.,” pp. 265-276.

43. Tay, A.O., Stevension, M.G., Davis, G., “Using the finite element method to determine temperature distributions in orthogonal machining,” Proc. Instn. Mech. Engrs Vol. 188(1974), pp. 627-638.

44. ASM Handbook, Vol. 9 (Ohio: ASM International, 1990), p. 247.

45. Ibid., p. 462.

46. Voorhees, H.R., Report on The Elevated-Temperature Properties of Aluminum and Magnesium Alloys (Philadelpha:American Society for Testing Materials, 1960).

47. Walton, C.F., Gray and Ductile Iron Castings Handbook (Gray and Ductile Iron Founders' Society, 1971).

48. Maykuth, D.J., Monroe, R.E., Favor, R.J. and Moon, D.R., Titanium Base Alloys: 6Al-4V Processes and Properties Handbook (Battelle Memorial Institute, 1971).

49. Physical metallurgy of Aluminum Alloys, (Cleveland: American Society for Metals, 1949), p. 78.

50. Horn, k.R.Van, Aluminum, Properties, Physical Metallurgy and Phase Diagrams (Ohio: American Society fro metals, 1967).

51. Ibid., p. 150.

52. Nayak, P.R., “Random Process Model of Rough Surfaces,” J. Lub. Tech., Trans. Of ASME, Vol. 93(1971), pp. 398-407.

53. Greenword, J.A. and Williamson, J.B.P. “Contact of Nominally Flat Surfaces,” Proc. R. Soc. London, Ser. A, Vol. 295 (1966), pp. 300-319.

54. Johnson, K. L., Contact Mechanics (London: Cambridge, 1985).

55. Wang S. and Komvopoulos, K., “A Fractal Theory of the Interfacial Temperature Distribution in the Slow Sliding Regime: Part I—Elastic Contact and Heat Transfer Analysis,” Journal of Tribology, Vol. 116(1994), pp. 812-823.

56. Webster, M.N. and Sayles, R.S., A Numerical Model for the Elastic Frictionless Contact of Real Rough Surfaces," Journal of Tribology, Vol. 108 (1986), pp. 314-320.

57. Yu, Y. and Zheng, L., "A Full Numerical Solution for Elastic Contact of Three-Dimensional Real Rough Surfaces," Wear, Vol. 157(1992), pp. 151-161.

58. Kim, K.W. and Sin, H.C., "Development of A Thermo-Viscoplastic Cutting Model Using Finite Element Method," International Journal of Machine Tools & Manufacture, vol. *36*(3) (1996), pp. 379-397.

59. Fernandez, J.E., Wang, Yinglong, Tucho, R., Martin-Luengo, M.A., Rgancedo, A.Rincon, "Friction and Wear Behavior of Plasma-Sprayed Cr2O3 Coatings against Steel in a Wide Range of Sliding Velocities and Normal Loads," Tribology International, Vol. 29(1996), pp. 333-343.

60. Whilehouse, D.J. and Archard, J.F., "The Properties of Random Surfaces of Significance in Their Contact," Proc. R. Soc., Ser. A, Vol. 316 (1970), pp. 97-121.

61. Black, J., Kopalinsky, E. M. and Oxley, P.L.B., "Sliding Metallic Friction with Boundary Lubrication: an Investigation of a Simplified Friction Theory and of the Nature of Boundary Lubrication," Wear, Vol. 137(1990), pp. 161-174.

62. Tay, A.O., Stevension, M. G. and Davis, G., "Using the Finite Element Method to Determine Temperature Distributions in Orthogonal Machining," Proc. Instn. Mech. Engrs., Vol. 188(1974), pp. 627-638.

63. Tao, Z. and Lovell, M., "Towards An Improved Friction Model in Material Removal Processes," Transactions of The NAMRI, Vol. 30 (2002), pp. 9-16.

64. Jawahir, I.S. and Luttervelt, C.A. van, "Recent Developments in Chip Control Research and Applications," Ann CIRP, Vol. 42(1) (1993), pp. 659-693.

65. Palmer, W.B. and Oxley P.L.B., "Mechanics of Metal Cutting", proc. Inst. Mech. Eng., Vol. 173 (1959), pp. 623-654.

66. Roth, R.N. and Oxley, P.L.B., "A Slip-line Field Analysis for Orthogonal Machining Based on Experimental Flow Fields," J. Mech. Eng. Sci., Vol. 14(1972), pp. 85-97.